Heterocoagulation as a Facile Route To Prepare Stable Serum Albumin-Nanoparticle Conjugates for Biomedical Applications: Synthetic Protocols and Mechanistic Insights

Kin Man Au* **and Steven P. Armes***

Department of Chemistry, The University of Sheffield, Brook Hill, Sheffield, South Yorkshire, S3 7HF, U.K.

ABSTRACT

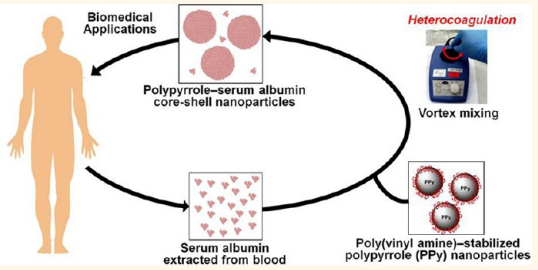

There is increasing interest in using serum albumin, the most abundant plasma protein, as a stabilizing agent in the context of nanomedicine. Using poly(vinyl amine)-stabilized polypyrrole nanoparticles as an example, we report a facile generic route to prepare serum albumin-nanoparticle conjugates *via* heterocoagulation. Time-resolved dynamic light scattering (DLS), disk centrifuge photosedimentometry (DCP), and circular dichroism (CD) spectroscopy studies confirm that bovine serum albumin (BSA) adsorbs rapidly onto the cationic poly(vinyl amine)-stabilized polypyrrole nanoparticles and suggest that the initial well-defined protein coronal is subsequently cross-linked *via* thiol-disulfide exchange. These BSA–nanoparticle conjugates were further characterized by X-ray photoelectron spectroscopy (XPS), aqueous electrophoresis, field emission scanning electron microscopy (FE SEM), and transmission electron microscopy (TEM). They exhibit excellent long-term colloidal stability under physiological conditions without further purification, suggesting strong irreversible adsorption by the BSA. Protein adsorption appears to be co-operative and both thermodynamic and mechanistic aspects were examined *via* aqueous electrophoresis, DCP, and DLS studies.

KEYWORDS: serum albumin · polypyrrole nanoparticles · protein adsorption · protein-nanoparticle interactions · heterocoagulation

Nanoparticles play an important role in medicine. Since the United States Food and Drug Administration (FDA) first approved the use of superparamagnetic iron oxide (SPIO) nanoparticles for ultrasound[1] and nuclear magnetic resonance imaging[2] in the mid-1990s, over a hundred nanomedicine clinical trials have been carried out around the world and more than 35 new nanomedicines have been granted FDA approval over the past 15 years.[3−6] Nevertheless, nanotoxicity and the rapid rejection of nanoparticles from the human body remain major challenges in nanomedicine.[7,8] In recent years, there is increasing interest in using a patient's own protein, such as serum albumin, as a stabilizing agent for nanoparticles in different medical applications because human protein can increase biocompatibility by reducing the chance of immune rejection and preventing non−specific build-up of nanoparticles inside the body.[9−14]

Serum albumin is the most abundant protein in the human body. Human whole blood contains 35−50 g/L of human serum albumin (HSA).[14−17] The two major functions of serum albumin are to maintain osmotic pressure between the intravascular system and body tissues and to transport fatty acids, hormones, bilirubin, and other small drug molecules throughout the body.[15,18,19] At physiological pH, the polypeptide chains are folded to form a heart-shaped conformation, with negative charges equally distributed in domains I and III (see Figure 1).[15,17,18] Isolation methods, such as cross-filtration,[20] have been developed to isolate serum albumin from blood for various biomedical applications, such as the treatment of hypovolemic shocks and acute liver failure.[21] Two serum albumin-based nanomedicines, namely 99m-technetium-labeled human serum albumin macroaggregates[22−24] and perflutren serum albumin microsphere (Optison),[25] were recently approved by the FDA for tumor imaging. The amino acid sequence of bovine serum albumin (BSA) is very similar to that of HSA. Moreover, these two proteins have almost identical

* Address correspondence to k.m.au@shef.ac.uk, s.p.armes@sheffield.ac.uk.

Received for review July 3, 2012 and accepted August 22, 2012.

Published online August 22, 2012
10.1021/nn302968j

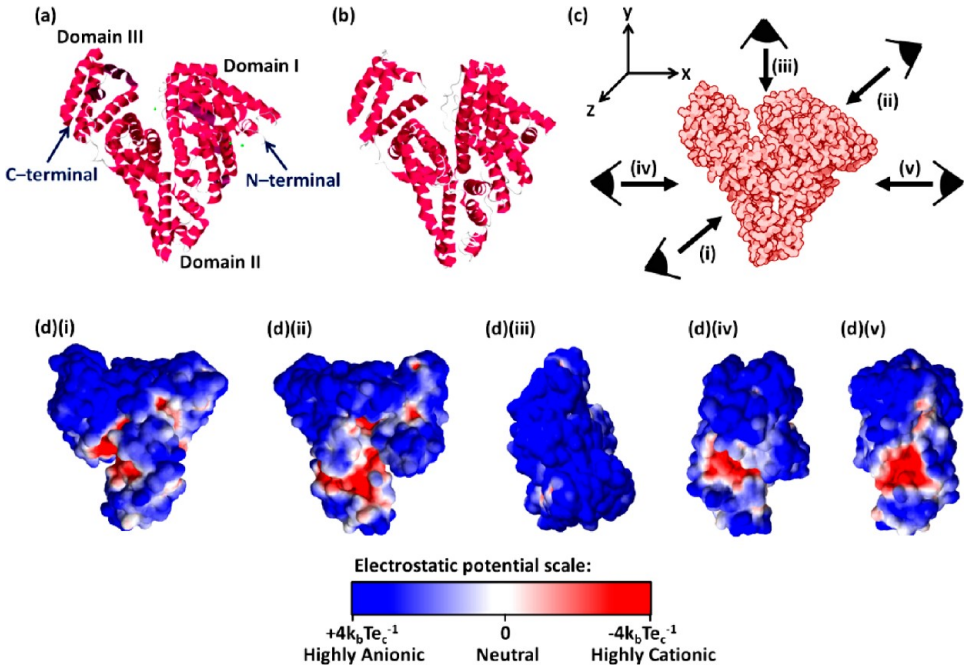

Figure 1. Crystal structure of serum albumin proteins. (a) X-ray crystal structure of bovine serum albumin (BSA) crystallized with calcium acetate (Protein Data Bank entry number 3V03). (b) X-ray crystal structure of human serum albumin (HSA) crystallized from poly(ethylene glycol) at a pH 7 (Protein Data Bank entry number 1AO6).[17] The secondary and tertiary structure of BSA is almost identical to that of HSA.[18] (c) Water-accessible space-filling model of human serum albumin 1AO6. BSA and HAS have almost identical "heart-shaped" tertiary structure with dimensions of 8 nm × 8 nm × 3 nm. (d) (i–v) Surface electrostatic potential distribution of human serum albumin 1AO6 at pH 7 observed from different directions, as calculated using the PDB2PQR surface charge distribution software package.[9,10] Negative, neutral, and positive potentials ranging from $-4k_bTe_c^{-1}$ (−103.4 mV) to $+4k_bTe_c^{-1}$ (+103.4 eV) are represented in blue, white, and red, respectively.

secondary and tertiary structures (see Figure 1).[18] Thus BSA has been widely used for various biomedical applications for decades.[22−25] Indeed, BSA has been used as an antiwrinkling agent in cosmetic products for more than half a century.[26] There is an increasing interest in using serum albumin in nanomedicine. This is partly because serum albumin can improve biocompatibility, but also because several studies have shown that serum albumin can improve the colloidal stability of nanoparticles as well.[9,12] In addition, several recent studies found that cancer cells selectively take up serum albumin-coupled drugs because tumors use this protein as a source of energy to maintain their high metabolic activity, whereas serum albumin−conjugated drugs do not enter healthy cells.[13,27−29] Thus serum albumin-coated nanoparticles are potentially useful in cancer diagnostics and therapies. However, depositing serum albumin onto nanoparticles can be challenging. The traditional covalent immobilization method often leads to irreversible aggregation and the resulting serum albumin−nanoparticle conjugates are often difficult to purify.[30,31] In recent years, much attention has focused on the physical adsorption of serum albumin onto cationic surfactant-stabilized nanoparticles, such as cetyltrimethylammonium bromide-stabilized gold sols,[9] iron oxide sols,[10,11] and gold nanorods.[13] Although preliminary *in vitro* studies are promising, this fabrication method has several drawbacks. First, an additional purification step is often required to remove free cationic surfactant, which is cytotoxic.[9−11,13,14] Second, the serum albumin layer thickness depends on the incubation period.[13] There are also concerns that such purified serum albumin-stabilized nanoparticles may aggregate when they encounter serum albumin in physiological fluids.[13] Furthermore, the serum albumin shell can slowly disintegrate in liposomal fluid, which regenerates the cytotoxic charge-stabilized nanoparticles.[13] Thus there is considerable scope for the development of a facile and general method to fabricate colloidally stable serum albumin-stabilized nanoparticles for nanomedicine.

Heterocoagulation is widely used to produce core−shell colloidal nanoparticles in ceramic composite processing indutries.[32−36] Heterocoagulation involves adsorption of small shell-forming particles (SFPs) onto the surface of larger, oppositely charged core-forming particles (CFPs). Unlike heteroflocculation, which is related to heterocoagulation but involves weaker reversible adsorption,[37−39] thermal annealing (*i.e.*, heating the initial core−shell nanoparticles above the glass transition temperature of the SFPs) is often required to prevent desorption of SFPs.[32−36] Most CFPs are sterically stabilized by polyelectrolytes (*e.g.*, poly(acrylic acid) (PAA), poly(vinyl amine) (PVAm), poly(ethylene imine) (PEI), poly(allylamine hydrochloride) (PAH)) to increase the colloidal stability of the CFPs and provide

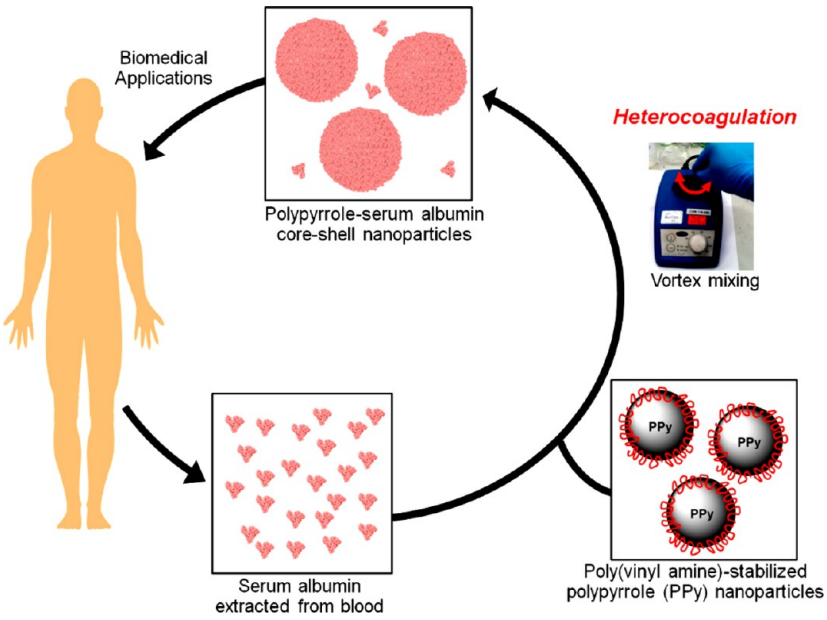

Scheme 1. Schematic representation of the concept of using protein-coated nanoparticles for biomedical applications. Serum albumin extracted from donor blood or patient's own blood can be used to fabricate biostable serum albumin-coated core–shell nanoparticles by heterocoagulation of the protein with polyamine-stabilized nanoparticles (*e.g.* poly(vinyl amine)-stabilized PPy nanoparticles are used in this work). Due to the non-toxic nature of non-adsorbed serum albumin, the biocompatible and highly colloidal stable serum albumin-stabilized nanoparticles can be used for biomedical applications without further purification.

an attractive electrostatic interaction with the SFPs. In some cases, the polyelectrolyte stabilizer also facilitates the adsorption of SFPs. Although heterocoagulation has been widely used in the ceramic industry for several decades, to the best of our knowledge this approach has not been used in biomedical applications. This may be due to our limited understanding of protein–cationic nanoparticle interactions[40–42] and the cytotoxic effects of polyelectrolytes.[8,34–43] We hypothesized that the presence of large patches of anionic charge on the surface of serum albumin (see Figure 1) and the well-known propensity of serum albumin to aggregate rapidly at high concentration[45,46] might enable the formation of a robust serum albumin coronal layer at the surface of cationic nanoparticles *via* heteroflocculation (Scheme 1) without requiring a subsequent annealing step. Such an adsorbed protein layer offers two potential advantages over traditional methods. First, electrostatic adsorption is usually very rapid,[39] which significantly reduces the fabrication time. Second, the as-made core–shell nanoparticles can be used immediately without further purification since any nonadsorbed serum albumin that may remain in aqueous solution is not cytotoxic. Hence in principle this approach allows the clinician to use the patient's own serum albumin to prepare serum-coated nanoparticles for point-of-care biomedical applications.

Polypyrrole (PPy) is an air-stable organic conducting polymer that was first discovered in the early 1960s.[47] Due to its excellent biocompatibility[48–50] and high electrical conductivity,[47] polypyrrole has been extensively investigated for various biomedical applications,[51,52] such as bioactuator, gas sensor, and substrate for manipulating mammalian cell growth and function. Polypyrrole nanoparticles can be readily prepared *via* aqueous dispersion polymerization of pyrrole using a mild oxidant such as iron(III) chloride in the presence of a suitable water-soluble polymeric stabilizer.[53–55] The stabilizer type dictates the surface chemistry and use of water-soluble copolymer stabilizers containing pendent thiophene or pyrrole moieties ensures chemical grafting onto the surface of the polypyrrole nanoparticles.[56–62] Such bespoke stabilizers can be designed to confer either anionic,[57,60] cationic,[62] zwitterionic, or nonionic character[56,58,59,61] on the polypyrrole nanoparticles. Recently, there is increasing interest in evaluating polypyrrole nanoparticles (and colloidal forms of related organic conducting polymers) for novel biomedical applications, such as marker particles for immunodiagnostic assays,[63] contrast agent for ultrasound tomography imaging,[64] magnetic resonance tomography imaging,[65] and optical coherence tomography imaging,[66] cell labeling,[67] photothermal therapy,[68] and drug delivery.[69]

Herein we use PVAm-stabilized polypyrrole (PPy) nanoparticles as a colloidal template to demonstrate the one-step fabrication of serum albumin-coated nanoparticles with a well-defined core–shell morphology *via* heteroflocculation. Dynamic light scattering (DLS) and disk centrifuge photosedimentometry (DCP) studies have been conducted to monitor the rate of BSA adsorption and the long-term stability of the resulting core–shell nanoparticles under physiological conditions. The thermodynamics of heterocoagulation and the structure of the BSA corona have also been studied using complementary characterization techniques. In principle, this fabrication

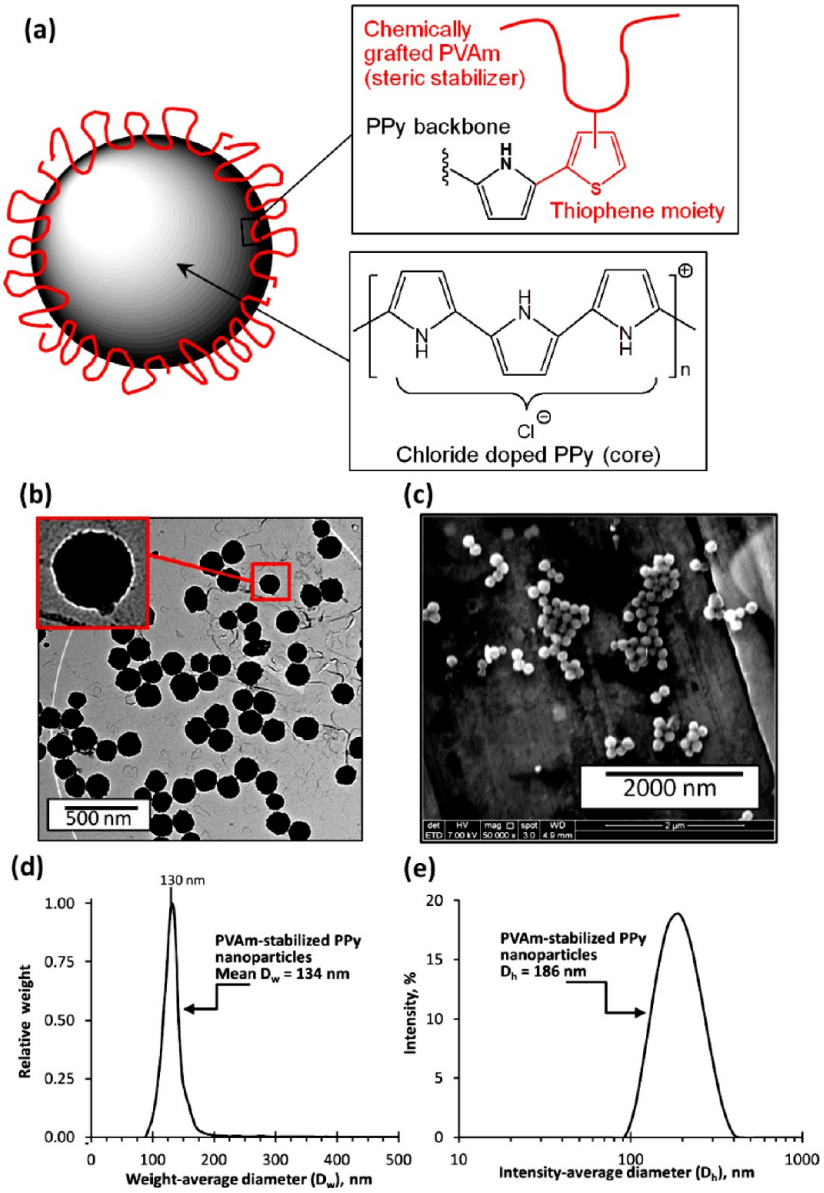

Figure 2. Characterization of PPy nanoparticles. (a) Cartoon illustration of the PVAm-stabilized PPy nanoparticles: the PVAm stabilizer chains are chemically grafted onto the PPy nanoparticle surface. (b) Representative TEM image recorded for PVAm-stabilized PPy nanoparticles. (c) Representative FE SEM image recorded for PVAm-stabilized PPy nanoparticles. The number-average particle diameter (D_n) was estimated to be 135 nm from digital image analysis of 102 nanoparticles (see Supporting Figure S1 for details). (d) DCP particle size distribution curve of the PVAm-stabilized PPy nanoparticles. The mean weight-average diameter (D_w) of the nanoparticles was 134 ± 24 nm. (e) DLS particle size distribution curve obtained for PVAm-stabilized PPy nanoparticles at 25 °C and pH 7. The intensity-average diameter (D_h) was 186 ± 43 nm (standard derivation based on the average of three 15 × 15 s measurements, SD = 3 nm).

technique should have generic applicability to many other polyamine-stabilized nanoparticles, including iron oxide and gold sols, quantum dots, polystyrene latexes, *etc.* To avoid interference from other plasma proteins and lipids,[12,70] we used highly purified bovine serum albumin (BSA, purified serum albumin extracted from bovine plasma) to replicate serum albumin corona.

RESULTS AND DISCUSSION

Synthesis and Characterization of Poly(vinyl amine)-Stabilized Polypyrrole Nanoparticles. PVAm-stabilized PPy nanoparticles were synthesized by aqueous dispersion polymerization using iron(III) trichloride as an oxidant in the presence of a reactive thiophene-functionalized PVAm stabilizer (see Figure 2a), as reported recently.[52,62] Briefly, a commercial sample of PVAm was reacted with 2-thiophenecarboxaldehyde followed by *in situ* reduction (see Materials and Methods for details). Figure 2 panels b and c show representative transmission electron microscopy (TEM) and field emission scanning electron microscopy (FE SEM) images recorded for the PVAm-stabilized PPy nanoparticles, which have a mean number-average particle diameter (D_n) of 134 nm (based on 159 particles counted from two micrographs,

see Supporting Figure S1(a)). This is reasonably consistent with the mean weight-average particle diameter (D_w) of 134 nm measured by DCP (Figure 2d) and the DLS intensity-average diameter (D_h) of 186 nm recorded, see Figure 2e. Comparing the number-average diameter of lyophilized PPy nanoparticles (where the steric stabilizer collapses to negligible thickness) with their intensity-average hydrodynamic diameter in aqueous solution, it is estimated that the upper limit of the thickness of solvated PVAm-stabilizing layer, $\delta_{h,max} = 0.5 \times (D_N - D_h) = 26$ nm. Comparing the microanalytical sulfur and nitrogen contents of the PVAm-stabilized PPy nanoparticles (S = 0.50 wt %, N = 16.4 wt %) with the nitrogen content of PPy bulk powder (N = 16.3 wt %) determined by elemental microanalysis, it is calculated that the purified PVAm-stabilized PPy nanoparticles contain 14.0 wt % PVAm stabilizer (surface grafting density, Γ = 5.5 mg m^{-2}), which is comparable with that of sterically stabilized PPy nanoparticles of similar particle diameter.[71] Based on the number-average diameter and steric stabilizer content of the PVAm-stabilized PPy nanoparticles and the bulk density of PPy bulk powder, the mean mass per PPy nanoparticle is calculated to be 2.21 $\times$ 10^{-15} g (see Supporting Figure S2 for the calculation). The surface sulfur-to-nitrogen atomic ratio of 0.10 determined by X-ray photoelectron spectroscopy (XPS) for these PVAm−stabilized PPy nanoparticles is 10 times higher than the corresponding S/N atomic ratio of 0.01 determined by elemental microanalyses (see Supporting Figure S3, Supporting Table S1), which strongly suggests that the hydrophilic PVAm stabilizer is present at the nanoparticle surface. The deconvoluted core-line S2p spectrum of the PVAm-stabilized PPy nanoparticles (see Supporting Figure S4) suggests that the pendent thiophene rings on the PVAm stabilizer are chemically grafted onto the PPy surface, since 64% of the sulfur atoms possess cationic character due to oxidation.[72] Aqueous electrophoresis studies indicate that the PVA-stabilized PPy nanoparticles has positive zeta potentials (+39.5 mV at pH 7 in 1 mM KCl; +13.5 mV at pH 7 in 0.1 M PBS) over the whole pH range investigated (see Supporting Figure S5). Given that the pK_a of PVAm is about 10,[73,74] these observations suggest that the cationic PVAm stabilizer is indeed located at the surface of the PPy nanoparticles, as expected. Although both PPy bulk powder (see Supporting Figure S5)[54] and charge-stabilized PPy nanoparticles[55] exhibit similar cationic character in the presence of 1 mM KCl at pH 7, their zeta potentials drop to about −12 mV when dispersed in 0.1 M PBS (also at pH 7), presumably due to compression of the electrical double layer (EDL) and adsorption of phosphate ions onto the PPy surface. This indicates that the cationic PVAm steric stabilizer is essential to maintain highly cationic character to ensure the strong electrostatic adsorption of anionic serum albumin in physiological buffer solution.

Preparation and Characterization of Serum Albumin−Polypyrrole Nanoparticle Conjugates. To a good approximation, proteins intercalate within the loosely packed solvated PVAm steric stabilizer layer and form a close-packed serum albumin corona after heterocoagulation. The upper limit for protein molecules (N_{max}) required to form a close-packed protein corona can be calculated using the following theoretical equation (see Remark S1 in Supporting Information for details),

$$N_{max} = \frac{\pi}{6}\frac{1}{V_p}[(D_N + 2\delta_{h,max})^3 - D_N^3] \quad (1)$$

where V_p is the volume of each serum albumin molecule (V_p of BSA = 83 nm^3, see remark S1 in Supporting Information for this calculation), D_N is the number-average nanoparticle diameter, and $\delta_{h,max}$ is the upper limit of the solvated steric stabilizer thickness. This theoretical equation allows precise estimation of the maximum number of proteins required to form a close-packed protein corona. In this particular case, the upper limit number of BSA molecules required to form a close-packed BSA corona on PVAm-stabilized PPy nanoparticles of 134 nm diameter is 24 500.

The efficient theranostic concentration of PPy nanoparticles (and closely related polyaniline nanoparticles) lies between 50 and 500 μg/mL.[66−68] To demonstrate that heterocoagulation can be used to prepare BSA-coated PPy nanoparticles at theranostic concentrations using a plasma-like concentration of serum albumin, 673 μM BSA (4.05 $\times$ 10^{17} BSA molecules per mL) in 0.1 M PBS was vortex-mixed with 50 to 1000 μg/mL PVAm-stabilized PPy nanoparticles (2.26 $\times$ 10^{10} to 4.52 $\times$ 10^{11} particles per mL) at 2000 rpm for 20 s (Scheme 1). It is perhaps worth emphasizing that the BSA/nanoparticle ratios in these experiments are well below the theoretical limit required to form well-defined core−shell nanoparticles calculated using eq 1. Figure 3a shows a representative TEM image of the heterocoagulated nanoparticles obtained using 200 μg/mL PVAm-stabilized PPy nanoparticles mixed with 673 μM BSA. The distinctive core−shell structure indicates the formation of a dense, space-filling protein layer. The image contrast between the PPy core and the BSA shell is due to the large electron scattering difference between these two components. There is also some evidence for nonadsorbed BSA in the TEM and FE SEM micrographs (see Figure 3a,b and Supporting Figure S1(b)). The particle size and colloidal stability of various BSA-coated PPy nanoparticles prepared under different conditions were characterized and monitored by DLS and DCP at 20 °C for 48 h (see Figure 3c and Supporting Figure S6(a) and (b)). The mean hydrodynamic diameter of the core−shell nanoparticles increased by approximately 20 nm after protein adsorption compared to the precursor PPy nanoparticles. The core−shell nanoparticles are relatively uniform in size. However, higher polydispersities were observed for samples prepared using either 50 or 100 μg/mL of PPy nanoparticles due to the large excess of nonadsorbed BSA, which is also

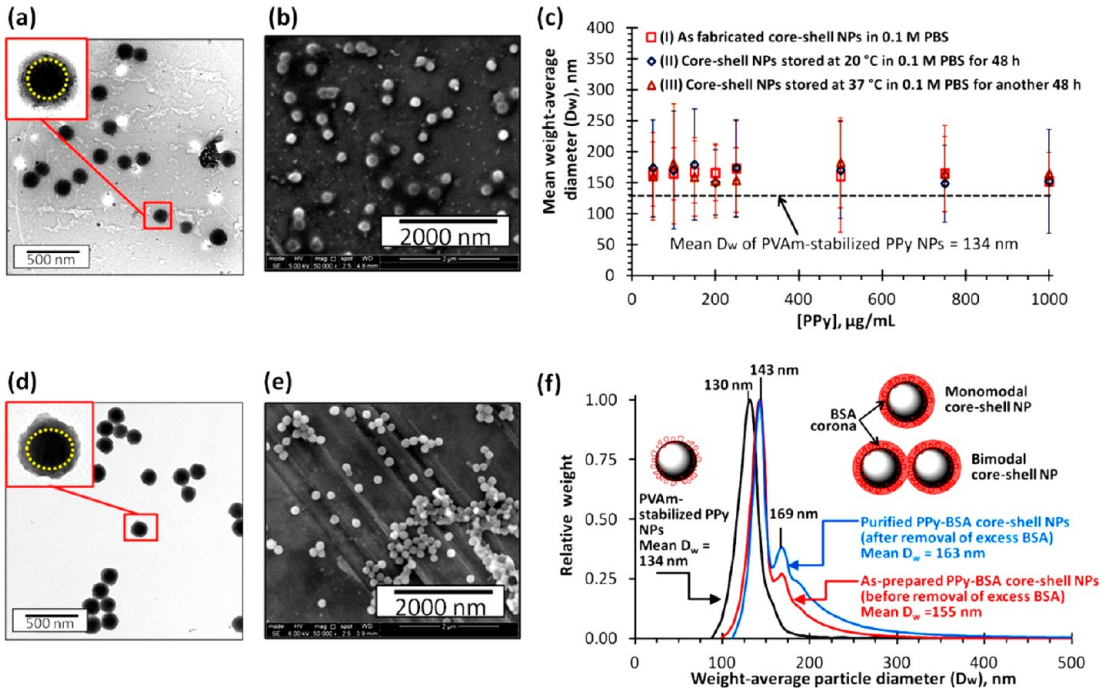

Figure 3. Particle size characterization of BSA–PPy nanoparticle conjugates. (a) Representative TEM image recorded for PPy–BSA core–shell nanoparticles (NPs) prepared using 200 μg/mL (9.05×10^{10} particles per mL) PPy nanoparticles. (b) Representative FE SEM image recorded for the PPy–BSA core–shell nanoparticles (NPs) prepared. (c) Weight-average diameter (D_w) of PPy–BSA core–shell nanoparticles as a function of PVAm-stabilized PPy nanoparticle concentration at a fixed BSA concentration of 673 μM. The mean D_w of the core–shell nanoparticles were recorded immediately after nanoparticle preparation (red open squares), after storage at 20 °C for 48 h (open diamonds), and after incubation at 37 °C for another 48 h (brown open triangles). The error bars represent the polydispersity of the core–shell nanoparticles. (d) Representative TEM image recorded for the PPy–BSA core–shell nanoparticles after six centrifugation–redispersion cycles. (e) Representative FE SEM image recorded for the PPy–BSA core–shell nanoparticles after six centrifugation-redispersion cycles. (see Supporting Figure S1 for particle size analyzes). (f) Weight-average particle diameter distribution curves recorded for the original PVAm-stabilized PPy nanoparticles (black curve), the as-prepared PPy–BSA core–shell nanoparticles obtained using 200 μg/mL PPy (red curve), and the purified PPy–BSA core–shell nanoparticles (blue curve). The modal diameters for the PVAm-stabilized PPy nanoparticles and for the two samples of PPy–BSA core–shell nanoparticles are 130, 143, and 169 nm, respectively.

detected by DLS (see Supporting Figure S6c). DLS measurements performed over 48 h confirmed that all core–shell nanoparticles prepared by heteroflocculation remained colloidally stable over the 48 h storage period (see Supporting Figure S6b), which suggests that it may be feasible for clinicians to prepare serum albumin-based core–shell nanoparticles prior to administration to patients.

DCP is a powerful method for characterizing particle size distributions of colloidal dispersions.[38,77–83] The weight-average diameter, D_w, increased from 134 nm (see Figure 3f) for the PVAm-stabilized PPy nanoparticles to around 155 to 164 nm for the BSA-coated PPy nanoparticles, (see Figure 3f). Moreover, these precursor nanoparticles invariably exhibited unimodal size distributions, whereas the BSA-coated nanoparticles typically displayed bimodal size distribution. The major population corresponds to the increase in particle diameter expected for the adsorbed shell of BSA.[81,82] The shoulder at higher diameter is at 169 nm, which is just under 20% greater than the *modal* diameter of 143 nm; this suggests the formation of doublets or dimers (see Remark S2(a) in Supporting Information for details).[84] In the above DCP analysis, the density of dried PVAm-stabilized PPy nanoparticles (ρ_{PPy} = 1.445 g cm^{-3}, as measured by helium pycnometry) was used to calculate the weight-average particle diameter. However, the addition of a hydrated BSA shell (ρ_{BSA} = 1.350 g cm^{-3})[85,86] will necessarily reduce the effective nanoparticle density, thus the *apparent* weight-average particle diameter will be smaller than the actual core–shell nanoparticle diameter if the original nanoparticle density of 1.445 g cm^{-3} is used. To address this problem, we applied an equation previously derived by Dawson *et al.* to correct for the core–shell density and hence (see Remark S2(B) in Supporting Information for details) calculated the actual BSA shell thickness (δw, BSA):[81,82]

$$\frac{(\rho_s - \rho_f)}{(\rho_c - \rho_f)}(D_{w,c} + 2\delta_w)^3 - D^2_{w,cs,app}(D_{w,c} + 2\delta_{w,BSA}) + \frac{(\rho_c - \rho_s)}{(\rho_c - \rho_f)} D^3_{w,c} = 0 \quad (2)$$

where ρ_c is the density of the particle core ($\rho_c = \rho_{PPy}$ = 1.445 g cm^{-3}), ρ_s is the shell density ($\rho_s = \rho_{BSA}$ = 1.350 g cm^{-3}),[85,86] ρ_f is the DCP spin fluid density (ρ_f of a 8 to 24% sucrose gradient = 1.064 g cm^{-3}, provided by CPS Instruments Ltd.),[87] $D_{w,c}$ is the D_w of unbound PPy

nanoparticles ($D_{w,c}$ = 130 nm), and $D_{w,cs,app}$ is the apparent D_w of the core–shell nanoparticles. Using the peak maximum of the particle size distribution curves of the PVAm-stabilized PPy nanoparticles and the major population for the BSA-coated PPy nanoparticles as references, the BSA coronal thickness ($\delta_{w,BSA}$) was calculated to be 9.5 nm, which is comparable to the BSA shell thickness determined by DLS ($\delta_{h,BSA}$ = 10.5 nm, see Supporting Figures S6a and b) and FE SEM ($\delta_{FESEM,BSA\text{-}shell}$ = 9 nm, calculated from the estimated difference in size between the PVAm-stabilized PPy and BSA-coated PPy nanoparticles, see Figures S1b and S1c in the Supporting Information). Time-dependent DCP studies (see Figure 3c and Supporting Figure S7) also confirmed the long-term colloidal stability of the unpurified BSA-coated PPy nanoparticles, since the major population remained constant at around 143 nm on storage at pH 7 over 48 h at 20 °C. In contrast, plasma protein-coated core–shell nanoparticles prepared by physical adsorption began to aggregate under similar physiological conditions within 2 h of their preparation.[88]

After storage at 20 °C for 48 h, the BSA-coated PPy nanoparticles were incubated at 37 °C for a further 48 h to mimic the physiological environment of human body. The colloidal stability of the core–shell nanoparticles was assessed by DCP (see Figure 3f and Supporting Figure S6a and b). The mean D_w of various nanoparticles remained essentially constant during this incubation period, suggesting little or no aggregation. Similar results were obtained using DLS (see Supporting Figure S6b). Most nonmetabolized nanoparticles are removed within 48 h after administration *via* excretion through the liver and kidney,[89] thus these data suggest that the protein-coated core–shell nanoparticles can be used for biomedical applications directly without further purification.

Colloidal Stability of BSA-Coated Polypyrrole Nanoparticles after Removal of Excess Nonadsorbed Protein. BSA-coated PPy nanoparticles prepared at 200 μg/mL were further examined to investigate the stability of the adsorbed protein layer in the absence of free protein. Thus nonadsorbed BSA was carefully removed *via* five centrifugation–redispersion cycles. Figure 3d shows a representative TEM image obtained for such purified BSA-coated PPy nanoparticles. A distinctive core–shell structure can again be observed, indicating that the BSA coronal layer remains intact. As shown in Figure 3f, the mean D_w (see also Figure S8a and b in Supporting Information for DLS data) of these purified nanoparticles slightly increased from 181 to 196 nm during purification: this weak flocculation may be at least partly due to inefficient redispersion after centrifugal sedimentation. However, the D_w values for the major and minor populations remained at 143 and 169 nm, respectively, suggesting that the BSA shell thickness remains essentially constant. The zeta potential of the purified BSA-coated PPy nanoparticles is −9.0 mV at pH 7 in 0.1 M PBS, which is comparable to that of both the unpurified nanoparticles and also BSA, which provides additional evidence that the protein remains adsorbed at the nanoparticle surface (see Figure 4a).[90−92] Identical heterocoagulation experiments were performed for another four times immediately after vortex mixing (20 s) to access the reproducibility of the fabrication method. As shown in Supporting Figure S9, the intensity-average diameter, weight-average diameter and zeta potential of the BSA-PPy nanoparticle conjugates recorded before and after removal of excess BSA are almost identical, suggesting that the heterocoagulation method is highly reproducible. XPS studies of the purified nanoparticles are also consistent with a thick layer of adsorbed protein. Figure 4b shows the C1s core-line XPS spectrum recorded for PVA-stabilized PPy nanoparticles, BSA, and purified BSA-coated PPy nanoparticles. Distinctive carbonyl features include –COOH at 288 eV and an amide carbonyl at 286 eV due to the peptidic residues of the BSA.[93,94] Peak deconvolution of this C1s core-line spectrum suggests that the BSA surface coverage is around 88%. Similarly, FTIR spectroscopy studies of the BSA-coated PPy nanoparticles reveal a strong amide I band at 1631 cm^{-1} and C–H stretching band at 1372 cm^{-1} contributed from the adsorbed BSA[95] although the amide band II at 1511 cm^{-1} and the amide band III at 1441 cm^{-1} overlap with the strong PPy bands at 1569 and 1460 cm^{-1} due to ν(C=C) and ν(C=N) respectively,[96] see Figure 4c. Spectroscopic measurements (see Figure 4d) indicate the fabrication of serum albumin corona and subsequent purification does not change the strong near-infrared absorption of the polypyrrole nanoparticles, which is essential for many biomedical applications, such as optical coherence tomography imaging.[66] Time-resolved DLS, aqueous electrophoresis, and DCP studies (see Supporting Figure S8a and c) also indicate that there is negligible desorption of the BSA chains from the PPy nanoparticle surface in the absence of free BSA in solution.

Colloidal Stability of BSA-Coated PPy Nanoparticles under Extreme Conditions. It is well-known that weakly bound noncross-linked proteins can be readily desorbed from polyelectrolyte-coated surfaces in the presence of either high ionic strength or ionic surfactant.[97] Thus salt and surfactant challenges were used to assess the colloidal stability of purified BSA-coated PPy core–shell nanoparticles (see Materials and Methods section for further details). Nanoparticles were exposed to either 1.0 M NaCl or 0.50 M SDS, sonicated for 30 min and then subjected to five centrifugation–redispersion cycles to remove any desorbed or weakly bound BSA. Colloidal stabilities of the nanoparticles were then assessed by DCP, DLS, and aqueous electrophoresis. As shown in Figure 5a, the peak maxima of the weight-average diameter distribution curves remained at 143 nm (main peak) and 169 nm (minor peak)

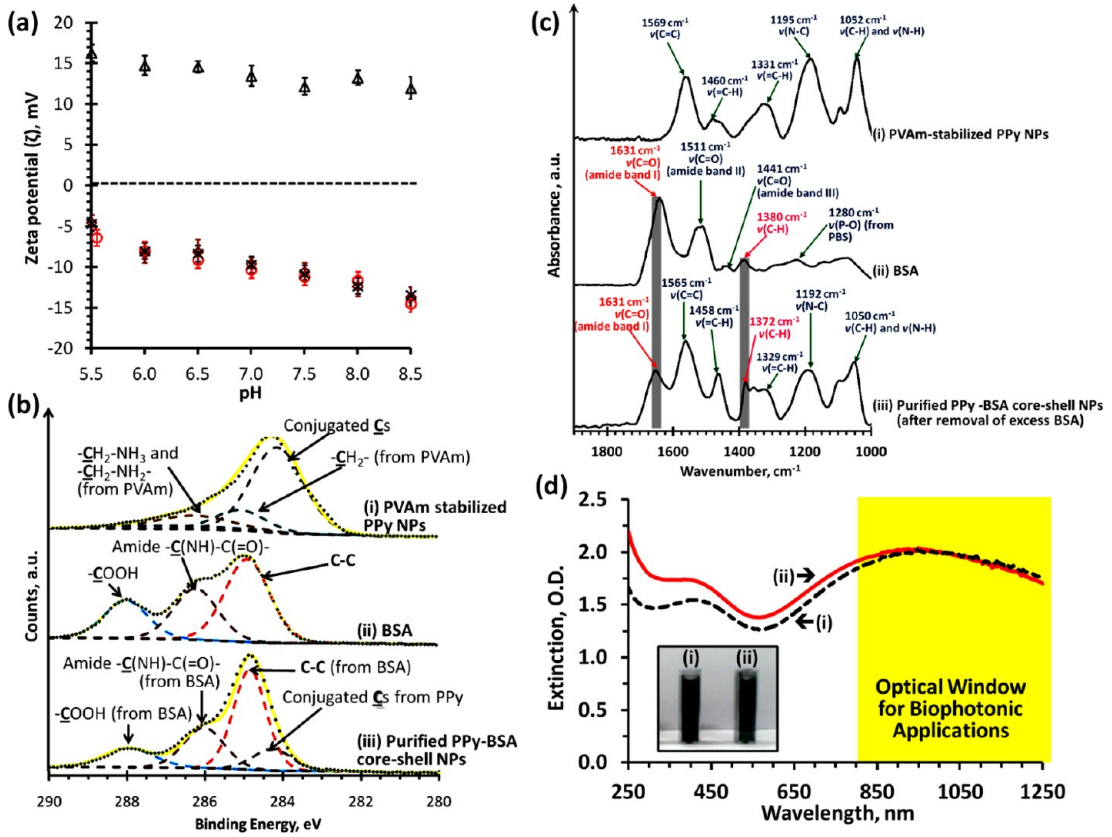

Figure 4. Evidence for the formation of a BSA coronal layer on the purified PVAm-stabilized PPy nanoparticles (NPs). (a) Aqueous electrophoresis curves recorded for (i) PVAm-stabilized PPy nanoparticles (Δ), (ii) BSA (○), (iii) as-prepared PPy−BSA core−shell nanoparticles obtained using 200 μg/mL PPy nanoparticles and 673 μM BSA (◇), and (iv) purified PPy−BSA core−shell nanoparticles (×) using 0.10 M PBS as background electrolyte. (b) Deconvoluted C1s core-line XPS spectra (with assignments) recorded for (i) PVAm-stabilized PPy nanoparticles, (ii) BSA, and (iii) purified PPy−BSA core−shell nanoparticles obtained using 200 μg/mL PPy nanoparticles and 673 μM BSA (after removal of excess BSA). Spectra were deconvoluted and assigned according to literature protocols.[93,94] N.B. The solid yellow lines represent best fits obtained after deconvolution. (c) Assigned ATR-FTIR spectra recorded after lyophilization for (i) PVAm-stabilized PPy nanoparticles, (ii) BSA (predissolved in 0.10 M PBS), and (iii) PPy−BSA core−shell nanoparticles after removal of excess nonadsorbed BSA *via* centrifugation. Spectra were assigned according to literature protocols.[95,96] (e) UV−visible−NIR extinction spectra recorded for 50 μg/mL dispersions of (i) PVAm-stabilized PPy nanoparticles (filled squares line) and (ii) purified BSA-PPy core−shell nanoparticles in 0.1 M PBS (solid red line). The strong and broad absorption band extending from the visible to NIR region is characteristics of the biopolaronic metallic state of doped polypyrrole.[53] The inset shows the digital micrograph of both PPy nanoparticles dispersions. The yellow highlighted region shows the NIR optical window for various potential biophotonic applications of the BSA-PPy core−shell nanoparticles.

suggesting the BSA corona thickness remained unchanged after the salt/surfactant challenges. The mean weight-average diameters (D_w) increased from 155 to 195 nm and 207 nm for the core−shell nanoparticles after salt and surfactant challenges due to inefficient redispersion after centrifugal sedimentation. Similarly in Figure 5b, the hydrodynamic particle diameter (D_h) of the core−shell nanoparticles increased from 205 nm to either 208 or 225 nm for the core−shell nanoparticles after the salt or surfactant challenges, respectively. The mean zeta potential of the core−shell nanoparticles after salt/surfactant challenges remained at about −9 mV (see Figure 5c), which suggests that the anionic BSA corona remains intact at the surface of the PVAm−PPy nanoparticles. These colloid stability studies indicate that the protein interacts strongly with the hydrated PVAm stabilizer chains, unlike the weak reversible protein adsorption previously observed for anionic polyelectrolyte-stabilized nanoparticles.[63] This suggests that the BSA has become cross-linked during heterocoagulation indicating that the cross-linked protein coronas surrounding the PVAm-stabilized PPy nanoparticles are highly robust and hence should survive under the demanding *in vivo* conditions observed in some previous studies.[13]

Thermodynamic Aspects of BSA Adsorption onto PPy Nanoparticles. The nanoparticle zeta potential (ζ), which is calculated from its electrophoretic mobility (μ) using the Smoluchowski equation ($\zeta = (\eta/\varepsilon\mathbf{E})\mu$, where η is the solution viscosity, ε is the electrical permittivity of the electrolyte, and $\mathbf{E}$ is the applied electric field), is very sensitive to protein binding.[90−92,98] The surface-adsorbed protein changes the zeta potential by charge compensating the cationic PVAm stabilizer chains and also shifting the shear plane of the nanoparticle. Like capillary electrophoresis,[98−103] aqueous electrophoresis

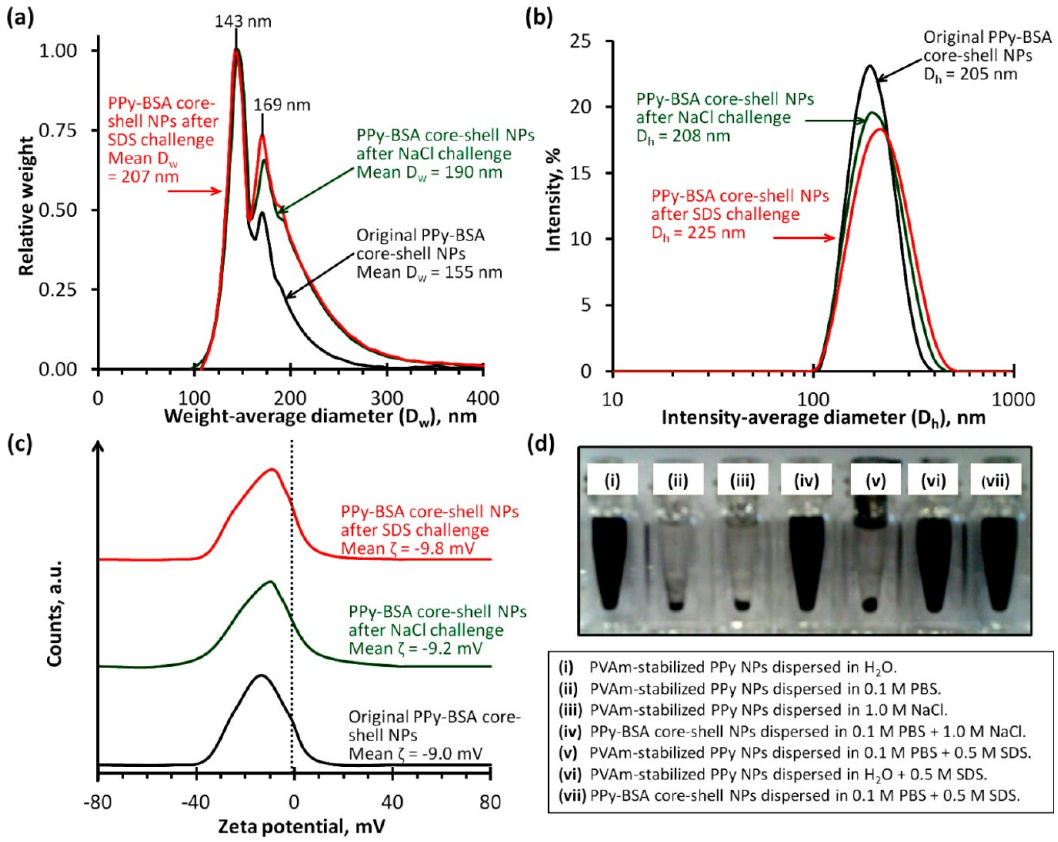

Figure 5. Colloidal stability of purified PPy−BSA core−shell nanoparticles after salt/surfactant challenges. (a) DCP curves for (i) the original purified PPy−BSA core−shell nanoparticles (black solid line), (ii) the same core−shell nanoparticles after an NaCl challenge (green solid line), and (iii) the same core−shell nanoparticles after an SDS challenge (red solid line). The mean D_w of the core−shell nanoparticles increased slightly after salt/surfactant challenges but the DCP modal diameters remained at 143 and 169 nm, which suggests that the shell thickness of the core−shell nanoparticles remained unchanged. (b) DLS size distributions and mean intensity-average diameters of (i) the original purified core−shell nanoparticles (black solid line), (ii) the same core−shell nanoparticles after an NaCl challenge (green solid line), and (iii) the same core−shell nanoparticles after an SDS challenge (red solid line) recorded at 25 °C in 0.10 M PBS. (c) Zeta potential (ζ) distributions and mean ζ values for (i) the original purified PPy−BSA core−shell nanoparticles (black solid line), (ii) the same core−shell nanoparticles after an NaCl challenge (green solid line), and (iii) the same core−shell nanoparticles after an SDS challenge (red solid line) using 0.10 M PBS (pH 7) as background electrolyte. (d) Digital micrograph recorded for 200 μg/mL PVAm-stabilized PPy nanoparticles dispersed in either (i) H_2O, (ii) 0.10 M PBS, (iii) 1.0 M NaCl solution, or (v) 0.50 M SDS solution, and also 200 μg/mL purifed PPy−BSA core−shell nanoparticles dispersed in 0.10 M PBS containing (iv) 1.0 M NaCl or (vii) 0.50 M SDS.

can be used to monitor protein−nanoparticle and nanoparticle−cellular interactions by measuring the change in electrophoretic mobility at equilibrium.[90−92] To investigate the thermodynamics of BSA adsorption, further aqueous electrophoresis studies were performed on a series of PPy nanoparticle−BSA conjugates prepared using 200 μg/mL (9.05×10^{10} particles per mL) of PVAm-stabilized PPy nanoparticles and BSA concentrations ranging from 0 to 1198 μM. The apparent zeta potential (ζ_{app}) of the BSA-coated PPy nanoparticles depends on their fractional saturation surface coverage by the BSA, such that:[98]

$$\zeta_{app} = \sum_{sat}^{k=0} f_k \zeta_k \qquad (3)$$

where f_k is the fraction of protein-bound conjugates of surface coverage k to reach its saturated surface coverage (*e.g.*, k = 0.35 when the protein-coated nanoparticles reach 35% of their saturated protein coverage) and ζ_k is the zeta potential of an individual protein−nanoparticle conjugate with surface coverage k. As shown in Figure 6a, the apparent zeta potential determined for the BSA-coated PPy nanoparticles is gradually reduced at higher BSA concentrations, because the adsorbed anionic BSA chains progressively neutralize the cationic PVAm stabilizer layer on the surface of the nanoparticles. The apparent zeta potential reaches a plateau (ζ_{sat} = −9.0 mV) when the BSA concentration is 1.5 μM, which corresponds to saturation adsorption. This indicates that about 9980 BSA molecules are adsorbed onto each nanoparticle. As shown in the Figure 6a inset, the peak width of the zeta potential distribution for the BSA-coated PPy nanoparticles increases at higher BSA concentrations, until a plateau value is attained which corresponds to saturation (full) coverage. Using the zeta potentials obtained for PVAm-stabilized PPy nanoparticles and BSA alone as references, the apparent zeta potential was converted into a fractional saturation

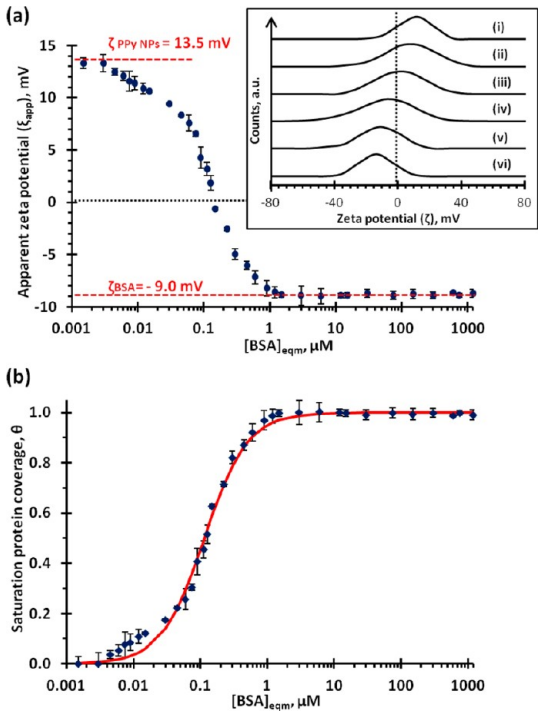

Figure 6. Thermodynamic aspects of BSA adsorption on the PVAm-stabilized PPy nanoparticles. (a) Apparent zeta potential (ζ_{app}) of core−shell PPy−BSA nanoparticles as a function of equilibrium BSA concentration. The inset shows representative zeta potential distribution curves recorded for (i) PVAm-stabilized PPy nanoparticles and PPy nanoparticle−BSA conjugates prepared using 200 μg/mL (9.05×10^{10} particles per mL) PVAm-stabilized PPy nanoparticles and a BSA concentration of (ii) 0.01 μM, (iii) 0.10 μM, (iv) 0.30 μM, and (v) 40 μM, and (vi) BSA alone in 0.10 M PBS background electrolyte. The error bars represent the standard deviation of each zeta potential measurement. (b) Saturated BSA coverage (θ) of the PVAm-stabilized PPy nanoparticles as a function of the BSA equilibrium concentration (black data points) and the best fit (red solid line) according to the Hill equation (see eq 4).

protein coverage (θ) using the following equation:[98]

$$\theta = \frac{\zeta_{app} - \zeta_{PPyNPs}}{\zeta_{sat} - \zeta_{PPyNPs}} \quad (4)$$

where ζ_{sat} is the zeta potential of the BSA-coated PPy nanoparticles obtained in the presence of excess BSA ($\zeta_{sat} = -9.0$ mV) and $\zeta_{PPy\ NPs}$ is the zeta potential of PVAm-stabilized PPy nanoparticles ($\zeta_{PPy\ NPs} = +13.5$ mV). The dependence of θ on BSA concentration was modeled using the Hill equation:[70,85,86,98,104−106]

$$\theta = \frac{[BSA]^{n_{Hill}}}{K_d^{n_{Hill}} + [BSA]^{n_{Hill}}} \quad (5)$$

where n_{Hill} is the Hill coefficient, [BSA] is the equilibrium BSA concentration, K_d is the microscopic dissociation constant (here K_d is defined as $1/K_a$, where K_a is the microscopic association coefficient). As shown in Figure 6b, BSA adsorption follows a Hill-type adsorption isotherm relatively well ($R^2 = 0.98$), yielding a dissociation constant of $K_d = 0.115 \pm 0.005$ μM (*i.e.*, $K_a = 8.70 \pm 0.38 \times 10^6$ M^{-1}). This relatively low K_d value suggests that BSA has a high binding affinity for the PVAm-stabilized PPy nanoparticles, as expected given the strong electrostatic interactions between anionic BSA and the cationic nanoparticles. The Hill coefficient ($n_{Hill} = 1.355 \pm 0.078$) obtained from the line of best fit is above unity, which is characteristic of a cooperative adsorption process.[70,76,85,86,98]

Mechanistic Insights for Serum Albumin Adsorption onto the Poly(vinyl amine)-Stabilized PPy Nanoparticles. The mechanism of serum albumin adsorption was further investigated by monitoring the change in particle diameter of the PVAm-stabilized PPy nanoparticles *via* DCP and DLS after they were equilibrated with varying concentrations (1.54−1.23 mM) of BSA. Figures 7a,b show the apparent mean weight-average diameter and intensity-average diameter observed for a 200 μg/mL (9.05×10^{10} particles per mL) dispersion of PVAm-stabilized PPy nanoparticles after equilibration with BSA for 1 min. Clearly, significant flocculation of the PVAm-stabilized PPy nanoparticles occurs in the presence of very low levels of BSA. For example, the apparent mean weight-average diameter and intensity-average diameter increased to 590 and 950 nm, respectively, when the nanoparticles were exposed to 1.5 nM BSA (BSA/PPy nanoparticle number ratio = 10), suggesting bridging flocculation.[107] The anionic domains I and III of BSA (see Figure 1 for the spatial location of these two domains) act as a bridge, joining two cationic PVAm-stabilized PPy nanoparticles together. FE SEM studies indicate the formation of large floccs (see the weight-average distribution curves (i) and (ii) in Figure 7c, and micrograph (i) in Figure 7d). Bridging flocculation has also been observed during the formation of polystyrene-silica core−shell nanoparticles *via* heteroflocculation in the submonolayer silica coverage regime.[108] As the BSA concentration increases, there is a concomitant reduction in the mean weight-average diameter, intensity-average diameter, and polydispersity. When the BSA concentration is increased to 62 nM (BSA/PPy nanoparticle number ratio = 412), the mean weight-average diameter and intensity average diameter are reduced to 340 and 430 nm, respectively, and relatively narrow particle size distributions are obtained by DCP (see curve (iii), Figure 7c), although most of the nanoparticles still exist as floccs (see micrograph (ii) in Figure 7d). Like the well-defined core−shell nanoparticles formed in the presence of excess BSA, the modal diameters in the weight-average distribution curve are at 143, 169, and 193 nm, which can be attributed to singlet, doublet, and triplet core−shell nanoparticles respectively (see Remark S2 in the Supporting Information for details). The apparent PPy nanoparticle diameter is further reduced when the equilibrium BSA concentration is increased to 1.5 μM (BSA/PPy nanoparticle number ratio = 9980), suggesting saturated absorption. As indicated by DCP and FE SEM (see micrograph (iii) in Figure 7d), the majority of nanoparticles exist as well-defined core−shell

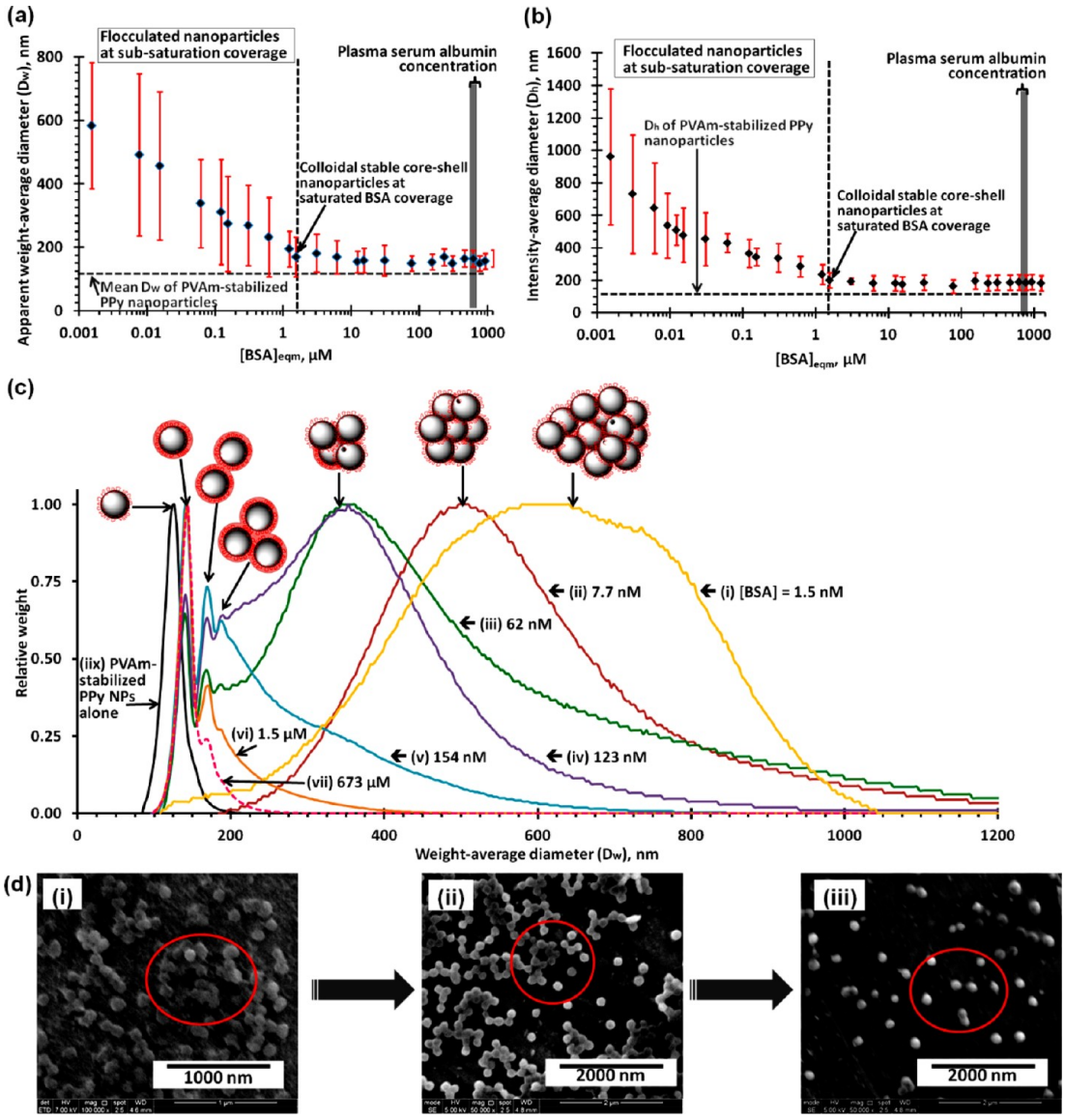

Figure 7. (a) Apparent weight-average diameter (D_w) of PVAm-stabilized PPy nanoparticles before and after equilibration with various concentrations of BSA, as judged by DCP. (b) Apparent hydrodynamic diameter (D_h) of PVAm-stabilized PPy nanoparticles before and after equilibration with various BSA concentrations. The yellow region shown in both plots represents the normal range expected for plasma serum albumin concentration. In both cases, a minimum particle diameter is attained at 1.5 μM BSA, which indicates saturated adsorption. Error bars indicate nanoparticle polydispersity, rather than experimental uncertainty. (c) DCP weight-average diameter distribution curves obtained for PVAm-stabilized PPy nanoparticles before and after equilibration with various concentrations of BSA. The inset cartoons depict the evolution of PVA-stabilized PPy nanoparticles from floccs to well-defined BSA-coated PPy nanoparticles in the presence of BSA. (d) FE SEM images recorded for as-prepared BSA-PPy conjugates after equilibration with (i) 1.5 nM BSA, (ii) 62 nM BSA, and (iii) 1.5 μM BSA. Large floccs observed in images (i) and (ii), see red circles, are due to nanoparticle aggregation. [Note: (1) The PVAm-stabilized PPy nanoparticle concentration was 200 μg/mL in all experiments. (2) All PVAm-stabilized PPy nanoparticles were equilibrated with BSA in 0.10 M PBS by vortex mixing at 2000 rpm for 20 s prior to the DCP and DLS measurements.].

nanoparticles under these conditions. As expected, there is little or no evidence for excess BSA in this FE SEM image, which was recorded without purification of the nanoparticles. The saturation BSA adsorption concentration indicated by DCP and DLS studies is consistent with that determined by aqueous electrophoresis. This suggests that each well-defined core–shell nanoparticle contains about 9980 BSA molecules. In addition, the number of BSA molecules required to form a closely packed coronal layer is calculated from the DCP and DLS data to be below the theoretical upper limit (N_{max}), thus demonstrating the validity of eq 1 for predicting the precise conditions required to form well-defined core–shell nanoparticles.

The conformation of adsorbed BSA in the purified PPy–BSA core–shell nanoparticles was assessed using far-UV circular dichroism (CD) spectroscopy.[109] Figure 8 shows CD spectra recorded for aqueous solutions/dispersions containing 375 nM native BSA, 375 nM thermally denatured BSA (prepared by heating BSA in 0.01 M HCl for 1 h),[110,111] 50 μg/mL PVAm-stabilized

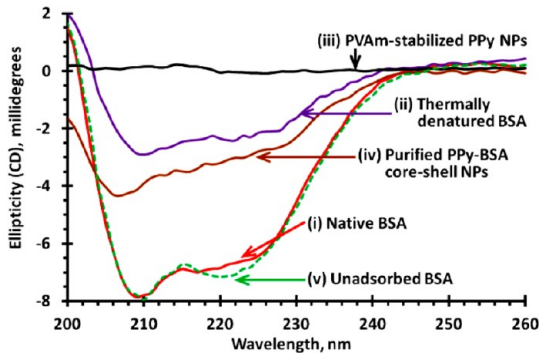

Figure 8. BSA conformation before and after adsorption onto PVAm-stabilized PPy nanoparticles. Circular dichroism (CD) spectra recorded for (i) 375 nM BSA in 0.10 M PBS, (ii) 375 nM thermally denatured BSA in 0.01 M HCl, (iii) 50 mg/mL PVAm-stabilized PPy nanoparticles, (iv) 50 mg/mL purified PPy−BSA core−shell nanoparticles dispersed in 0.10 M PBS (prepared *via* heterocoagulation of 200 μg/mL PVAm-stabilized PPy nanoparticles with 673 μM BSA in 0.10 M PBS), and (v) 375 nM nonadsorbed BSA in 0.10 M PBS (isolated from the purification of the PPy−BSA core−shell nanoparticles). The purified PPy−BSA core−shell nanoparticle dispersion and nonadsorbed BSA were diluted to the desired concentration (confirmed by UV−visible absorption spectroscopy) prior to the CD measurements. All CD spectroscopic measurements were performed at 37 °C using a 2 mm path length quartz curet.

PPy nanoparticles, 50 μg/mL purified PPy−BSA core−shell nanoparticles (prepared by mixing 200 μg/mL PVAm-stabilized PPy nanoparticles with 673 μM BSA), and 375 nM nonadsorbed BSA isolated during the purification of the PPy−BSA core−shell nanoparticles, respectively. On the basis of the aforementioned aqueous electrophoresis, DCP and DLS studies, the 50 μg/mL purified PPy−BSA nanoparticles contain the same number of BSA molecules as a 375 nM solution of BSA alone. As shown in the CD spectra, the local elliptic minimum for native BSA at 210 nm was blue-shifted to 206 nm after its adsorption onto the PVAm-stabilized PPy nanoparticles. A second characteristic local elliptic minimum for native BSA at 221 nm was no longer observed after adsorption, suggesting that BSA becomes partially/fully unfolded at the nanoparticle surface.[110−112] Quantitative analysis of the CD spectra using the self-organization map circular dichroism (SOMCD) protein secondary structure algorithm[113] (see Table 1 for details) revealed that the α-helix content of BSA is reduced from 79% to 64%, while the random coil composition slightly increased from initially around 15% up to 23% after adsorption onto the nanoparticles (compared to 33% α-helix and 29% random coil in the thermally denatured BSA), again suggesting that the adsorbed BSA partially unfolds but is not completely denatured. The conformation change can be explained by a modest change in the BSA conformation on adsorption in order to maximize a favorable electrostatic interaction, since the nanoparticle curvature is relatively small compared with the BSA dimensions. Similar partial unfolding of proteins has been observed when small, flexible cationic proteins (*e.g.*, chymotrypsin, ribonuclease) adsorb onto large anionic nanoparticles (*e.g.*, carboxylic acid-functionalized gold nanoparticles or anionic silica sols).[114−117] In addition, the SOMCD calculation revealed that adsorbed BSA comprises around 8% β-sheet, whereas native BSA contains zero β-sheet. This suggests local aggregation of the BSA,[112] which may arise from the high local BSA concentration at the nanoparticle surface facilitating intermolecular thiol-disulfide interchange between the sulfhydryl group on the free cysteine residue, Cys-34 (pK_{SH} = 5), near the N-terminus of the peptide chain in domain I with the 17 disulfide bonds on adjacent adsorbed BSA molecules.[45,46] Although the BSA molecules became partially deformed on adsorption, CD studies confirmed that the conformation of nonadsorbed BSA molecules remained unchanged, suggesting that removal of any nonadsorbed serum albumin molecules may be unnecessary for potential biomedical applications.

TABLE 1. The Relative Percentage of Protein Secondary Structures in Native BSA, Thermally-Denatured BSA, Purified PPy−BSA Core−shell Nanoparticles and Nonadsorbed Excess BSA Calculated from the Corresponding CD Spectra Using the Self-Organization Map Circular Dichroism (SOMCD) Protein Secondary Structure Algorithm

	relative percentage of protein secondary structure			
	α-helix, %	β-sheet, %	β-turn, %	Random coil, %[b]
native BSA	79.2	*a*	6.3	14.5
thermally denatured BSA	33.1	26.1	11.7	29.1
PPy−BSA core−shell nanoparticles	63.5	8.2	5.5	22.8
nonadsorbed BSA	78.6	*a*	6.4	15.0

[a] Both native BSA and nonadsorbed BSA contain a negligible amount of the β-sheet conformation. [b] Random coil % = 100% − α-helix % − β-sheet % − β-turn %.

On the basis of the collective experimental evidence and a serum albumin-poly(allylamine) surface adsorption model proposed by Schaaf *et al.*,[118] a serum albumin heterocoagulation mechanism is proposed in Figure 9. In physiological buffer (0.10 M PBS, pH 7.0), the chemically grafted PVAm chains ($pK_a \approx 10$)[73,74] become highly protonated to form solvated cationic loops.[119] At a very low BSA equilibrium concentration, the anionic domains I and III of BSA (see Figure 1) have a high binding affinity for the nanoparticles. Since BSA has a heart-shaped tertiary structure, the two anionic domains can bind to neighboring nanoparticles. When such adsorption occurs, it leads to bridging flocculation of the nanoparticles. At higher BSA concentrations, the adsorbed BSA molecules charge compensate the cationic PVAm stabilizer chains and form a well-defined dense protein shell. The cooperative nature of the adsorption mechanism is confirmed by aqueous electrophoresis studies, since the Hill coefficient for BSA adsorption exceeds unity ($n_{Hill} > 1$). Such adsorption

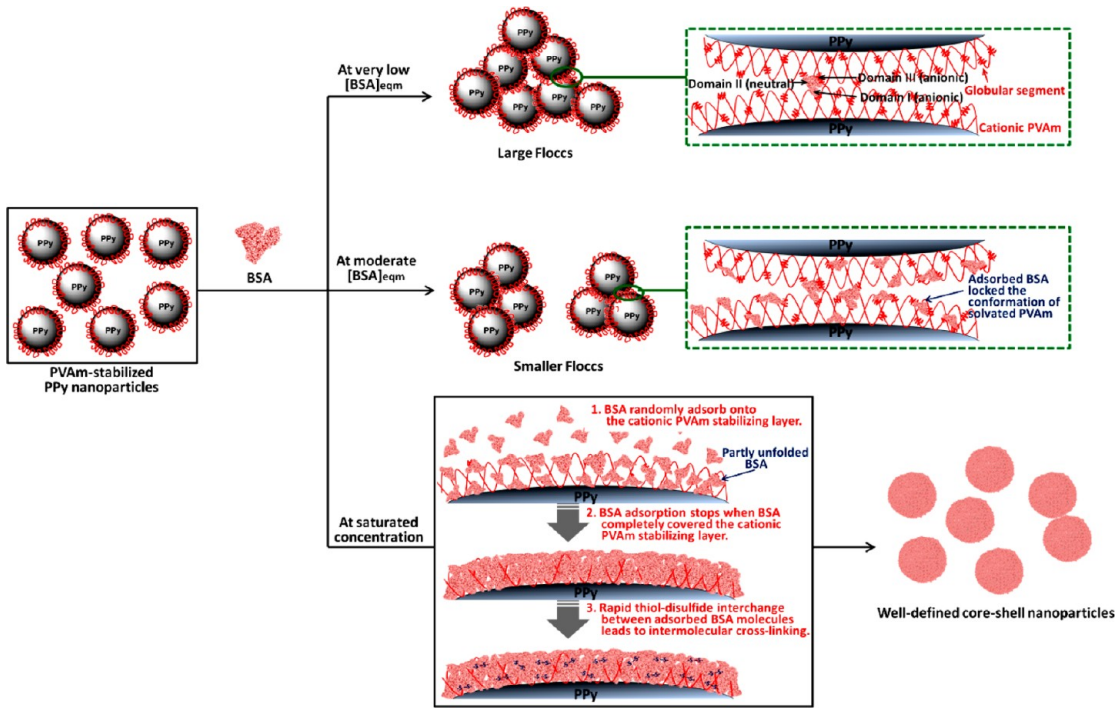

Figure 9. Schematic illustration of the proposed mechanism for BSA adsorption onto PVAm-stabilized PPy nanoparticles. At low BSA concentration, the anionic domains I and III of BSA act as a bridge and allow the protein to adsorb onto neighboring nanoparticles, which leads to flocculation. At higher BSA concentration, more protein molecules can enter the cationic PVAm stabilizer layer and randomly adsorb onto the PPy nanoparticles. No further adsorption occurs when BSA completely covers the nanoparticles. BSA molecules within the dense protein shell then undergo thiol-disulfide interchange, leading to intermolecular cross-linking and the formation of a rigid serum albumin corona at the surface of the PPy nanoparticles. (Note: Each BSA molecule has 35 cysteine residues.[15,17] Under physiological conditions, 34 cysteine residues are in their dimerized stable form (*i.e.*, as 17 disulfide bonds).[15,17] Approximately 99% of the single free cysteine residues, Cys-34 (pK_{SH} = 5), are deprotonated at physiological pH. At a sufficiently high local concentration, these deprotonated Cys-34 residues undergo a rapid intermolecular thiol-disulfide interchange cross-linking reaction with the disulfide bridge of neighboring protein molecules[45,46]).

is both enthalpically driven (due to the favorable electrostatics) and also entropically driven,[101] because adsorption of a relatively large BSA molecule displaces many surface-bound water molecules so there is an overall increase in disorder. Higher BSA concentrations also reduce the probability of bridging flocculation because there is a greater likelihood that the nanoparticles interact with free BSA molecules, rather than with partially adsorbed BSA. As a result, the apparent mean nanoparticle diameter is reduced. It is also important to note that BSA adsorption should be self-limiting in the presence of excess BSA, since it is constrained by the thickness of the solvated PVAm stabilizer chains. This is confirmed by the constant BSA shell thickness determined by DCP after PPy nanoparticles are mixed with excess BSA (see curves (vi) and (vii) in Figure 7c). Finally, the high local BSA concentration at the nanoparticle surface facilitates thiol-disulfide exchange between adjacent adsorbed BSA molecules and covalently stabilizes the adsorbed protein layer, thus preventing its desorption either at high ionic strength or when subjected to a surfactant challenge. Evidence for the cross-linking mechanism between adsorbed BSA molecules is provided by the observation of 8% β-sheet formation, as indicated by CD spectroscopy. Other workers have inferred that significant structural order can arise at submonolayer coverage on the basis of both experimental data[120] and molecular modeling.[121] However, for the specific case of BSA adsorption onto PVAm-stabilized PPy nanoparticles there seems to be no evidence for such behavior.

CONCLUSIONS

In summary, a standard plasma concentration of serum albumin (634 μM) is sufficient to allow the efficient preparation of serum albumin-coated polypyrrole nanoparticles in the theranostic concentration regime (below 1000 μg/mL) *via* heterocoagulation. Time-dependent DLS and DCP studies indicate the formation of an adsorbed serum albumin coronal layer of around 10 nm immediately after vortex mixing, confirming rapid protein adsorption onto cationic polyamine-stabilized nanoparticles. In addition, these as-fabricated core−shell nanoparticles exhibit excellent colloidal stability under both ambient and physiological conditions (37 °C, 0.1 M PBS, pH 7) over time scales of weeks. Unlike previous reports,[81,85−89] there is no evidence for protein desorption or nanoparticle aggregation under extreme conditions (*e.g.*, at high salt content or in the presence of surfactant). This is

attributed to intermolecular cross-linking between adsorbed adjacent protein molecules *via* thiol-disulfide exchange. Aqueous electrophoresis studies of serum albumin-coated PPy nanoparticles conjugates confirms that protein absorption is co-operative (Hill coefficient, $n_{Hill} > 1$) with a submicromolar binding affinity (association constant, $K_a = 8.7 \pm 0.4 \times 10^6\ M^{-1}$). Further mechanistic studies indicate that PVAm-stabilized nanoparticles undergo bridging at the subsaturated coverage regime, where the two anionic serum albumin domains act as a bridge joining the nanoparticles together. However, the upper limit of serum albumin required to form well-defined core−shell nanoparticles can be calculated from theory. Moreover, circular dichroism studies provide direct evidence for covalent stabilization of the adsorbed BSA molecules *via* thiol-disulfide exchange, which is consistent with the excellent long-term colloidal stability exhibited by these core−shell nanoparticles. The heterocoagulation technique reported herein is expected to be of generic utility for the facile preparation of serum albumin-coated nanoparticles for various biomedical applications, such as medical imaging, photothermal therapy, and drug delivery. In principle, this approach also provides opportunities for the fabrication of other protein−nanoparticle conjugates, such as antigen-coated nanoparticles for point-of-care *in vitro* immunodiagnostic assays.

MATERIALS AND METHODS

Chemicals and Materials. High molecular weight linear PVAm (Lupamin 9095, MW ≈ 340 000, degree of hydrolysis = 90%, obtained from a poly(*N*-vinyl formamide) precursor)[122,123] was donated by BASF (Ludwigshafen, Germany) as a concentrated aqueous solution. The solids content of this solution was determined using a moisture analyzer balance (Ohaus MB45), and the degree of hydrolysis was quantified by ^{1}H NMR spectroscopy prior to functionalization using 2-thiophenecarboxaldehyde (see Supporting Figure S10). Pyrrole (>98%) was purchased from Aldrich and purified by column chromatography (activated basic alumina stationary phase) and stored at −20 °C in the dark before use. Iron(III) trichloride hexahydrate (ACS reagent, 98.0−102%), 2-thiophenecarboxaldehyde (98%), and bovine serum albumin (BioXtra) were purchased from Aldrich and used without further purification. Sodium dodecyl sulfate (SDS) was purchased from VWR International Ltd., AmberliteIRA400 (hydroxide form anion exchange resin) was purchased from Aldrich and was eluted with copious amounts of doubly deionized water before use. Methanol and sodium borohydride (reagent grade) were obtained from Fisher Scientific. Dialysis membrane (MWCO ≈ 1000 Da) was purchased from Spectrum. Phosphate-buffered saline (PBS) tablets were purchased from Oxoid Ltd. (U.K.). Each 0.10 M PBS solution contains 137 mM sodium chloride (NaCl), 2.7 mM potassium chloride (KCl), 10 mM disodium phosphate (Na_2HPO_4), and 1.76 mM potassium dihydrogen phosphate (KH_2PO_4). Thus the ionic strength of 0.10 M PBS is equivalent to the ionic strength of 0.153 M NaCl.

Functionalization of Poly(vinyl amine) with 2-Thiophenecarboxaldehyde. 2-Thiophene-functionalized PVAm was synthesized by the one-pot reductive amination from commercially available PVAm (Lupamin9095).[105]The *N*-vinylformamide unit (due to incomplete hydrolysis of poly(*N*-vinyl formamide))[103,104] was also reduced using excess $NaBH_4$ to form *N*-vinylmethyl amine during reductive amination (Scheme 2).[106] Approximately 81 mol % of the repeat units in the functionalized PVAm chains comprise primary amines, with the remaining 19 mol % being secondary amines. Briefly, PVAm solution (20.00 g, solids content = 28.50%, 27.50 mmol primary amine) was diluted with H_2O (60 mL) in a 250 mL round-bottomed flask equipped with a magnetic stirrer. The pH of the solution was adjusted to pH 10.0 by 1.5 M NaOH. After the solution was stirred at 20 °C for 30 min, 2-thiophenecarboxaldehyde (308 mg, 2.75 mmol) in methanol (10 mL) was added to the PVAm solution and stirred at 20 °C for 4 h. Excess sodium borohydride (1.50 g, 0.48 mol) was added to the reaction mixture slowly and stirred at 20 °C for 18 h to reduce the imine intermediate. HCl (1.5 M, 15 mL) was added dropwise to the reaction mixture to quench the unreacted sodium borohydride. The functionalized PVAm was purified by equilibrium dialysis against deionized water for 1 week (15 cycles). The copolymer was further purified to remove sodium formate, which is the major impurity in the commercially available Lupamin9095, by passing through an anion exchange column (AmberliteIRA400, hydroxide form anion exchange resin) before being freeze-dried from water overnight. ^{1}H NMR (400 MHz, D_2O, 25 °C) δ: 7.40 (s), 6.95 (s), 4.00 (s), 3.20 (s), 3.00 (s), 1.65 (s) (see Supporting Figure S10). IR (ATR, cm^{-1}): 3126, 3268 (broad, N−H stretching), 3166 (weak, =C−H stretching), 2850 (strong, −C−H stretching), 1589 (very broad, N−H stretching and C=C stretching), 1437 (C−H stretching), and 1375 (C−H stretching from CH_3). Elemental analysis calcd. C: 56.63, H: 10.58, N: 26.37, S: 5.42. Found: C, 54.35; H, 9.41; N, 29.85; S, 4.51%.

Synthesis of Poly(vinyl amine)-Stabilized Polypyrrole Nanoparticles. PVAm-stabilized PPy nanoparticles were prepared *via* aqueous dispersion polymerization, as previously reported (Scheme 3).[55] Briefly, 2-thiophene-functionalized PVAm (0.50 g) and iron(III) trichloride hexahydrate (9.10 g, 33.7 mmol) were separately dissolved in 80 and 20 mL of deionized water, respectively. The iron(III) trichloride solution and pyrrole (1.00 mL, 14.4 mmol) were added to the stirred copolymer stabilizer solution. Polymerization was allowed to proceed at 20 °C for 18 h. The resulting black dispersion was first filtered through prewashed glass wool under gravity, before being centrifuged at 15000 rpm for 2 h and the resulting black sediment was redispersed in deionized water with the aid of ultrasonication for 1 to 2 h. This centrifugation−redispersion cycle was repeated eight times. Purified polypyrrole nanoparticles were filtered through prewashed glass wool to remove any aggregated particles before further studies. The solids content of the PPy nanoparticles was assessed using a moisture analyzer. Bulk density (measured by helium pycnometry): 1.445 g cm^{-3} at 20 °C. Elemental analysis, found: C = 55.22%; H = 3.89%; N = 16.41%; Cl = 10.31%; S = 0.50%. In a control experiment, the attempted synthesis of PVAm-stabilized PPy nanoapticles using nonthiophene-functionalized PVAm (at 5.0 wt/v % concentration) was unsuccessful, since a macroscopic PPy bulk powder precipitate was formed within 10 min of the polymerization.

Synthesis of PPy Bulk Powder[126]. Iron(III) trichloride hexahydrate (9.10 g, 33.7 mmol) was dissolved in deionized water (100 mL) in a 125 mL sealed container with constant stirring. After 30 min, pyrrole (1.00 mL, 14.4 mmol) was added to this iron chloride solution *via* syringe. Polymerization was allowed to proceed for 24 h at 20 °C. The resulting PPy bulk powder was purified by washing with copious amounts of deionized water in a filter funnel and dried at 50 °C for 24 h before further studies. Bulk density (measured by helium pycnometry): 1.510 g cm^{-3} at 20 °C. Elemental analysis, found: C = 55.09%; H = 3.16%; N = 16.30%, Cl = 10.68%.

Fabrication of PPy−BSA Core−Shell Nanoparticles by Heterocoagulation. PPy−BSA core−shell nanoparticles were fabricated by vortex-mixing 634 μM BSA in 0.10 M PBS (pH 7) with 50 to 1,000 μg/mL of PVAm-stabilized PPy nanoparticles at 2000 rpm for 20 s. In selected samples, excess BSA molecules were removed by five centrifugation (10 000 rpm/25 min)−redispersion cycles prior to further studies.

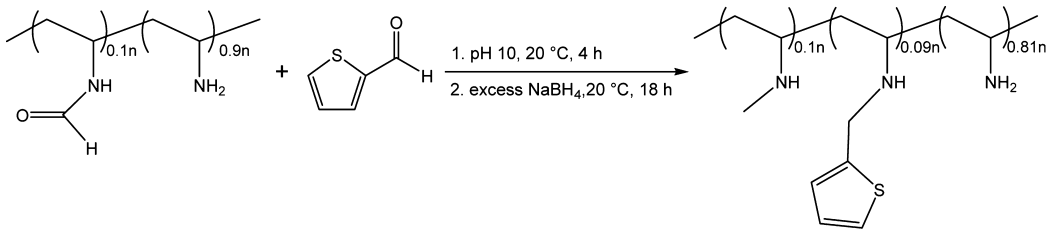

Scheme 2. Functionalization of the pendent amine groups on PVAm with 2-thiophenecarboxaldehyde *via* reductive amination.

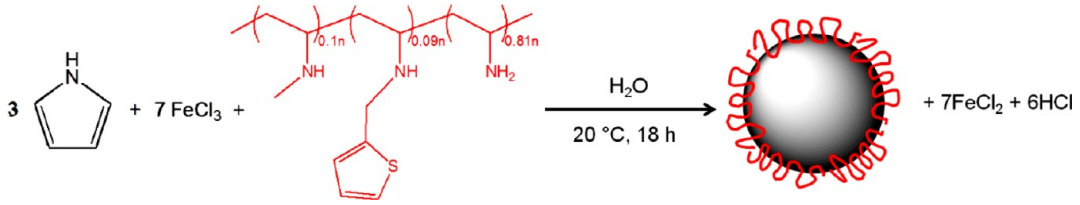

Scheme 3. Synthesis of PVAm-stabilized PPy nanoparticles *via* aqueous dispersion polymerization of pyrrole using iron(III) trichloride oxidant in combination with 2-thiophene-functionalized PVAm as a reactive steric stabilizer.

Characterization. *^{1}H NMR Spectroscopy.* All ^{1}H NMR spectra were recorded in D_2O or CD_3OD using a Bruker Avance 400 MHz NMR spectrometer operated at 25 °C using solvent residual peak(s) as internal reference. NMR spectra were processed using MestReNova (version 7.10, MestreLab Research S.L.).

FT-IR Spectroscopy. PVAm-stabilized PPy nanoparticles, BSA solution (in 0.10 M PBS), and purified PPy–BSA core–shell NPs were each freeze-dried overnight prior to analysis. Analyses were conducted using a Nicolet iS10 FT-IR spectrometer equipped with an attenuated total reflectance (ATR) accessory. The spectral resolution was 4 cm^{-1} and 128 scans were averaged per spectrum.

UV–Visible-NIR Spectroscopy. UV–visible–NIR extinction spectra of different polypyrrole nanoparticles dispersion were recorded using a double-beam Perkin-Elmer Lambda 900 UV–vis–NIR spectrometer at 20 °C using either deionized water or 0.1 M PBS as reference.

Dynamic Light Scattering (DLS). Dynamic light scattering studies were conducted at 37, 25, or 2 °C using a Malvern Zetasizer Nano ZS instrument equipped with a 4 mW He–Ne solid-state laser operating at 633 nm. Backscattered light was detected at 173° and the intensity-average hydrodynamic diameter (D_h) was calculated over 15 runs (each of 15 s duration) from the quadratic fitting of the correlation function using the Stokes–Einstein equation. All measurements were performed in triplicate.

Aqueous Electrophoresis. These measurements were conducted using the same Malvern Zetasizer Nano ZS instrument described above using slow field reversal (SFR) and fast field reversal (FFR) phase analysis light scattering (M3-PALS) technique with either 1 to 200 mM NaCl or 0.10 M PBS as background electrolyte. Zeta potentials were calculated from electrophoretic mobilities using the Smoluchowski relationship. The solution pH was adjusted manually by the addition of either dilute HCl or NaOH solution. The zeta potential of PPy bulk powder was measured using the protocol reported in reference 75. All measurements were performed in triplicate.

All light scattering data (dynamic light scattering and aqueous electrophoresis) were processed using Malvern Zetasizer Software version 6.20. The viscosity and dielectric constant of 0.1 M PBS, and different concentrations of NaCl solutions were either provided by Malvern Ltd. (UK) or calculated using Malvern Zetasizer Software version 6.20.

Disk Centrifuge Photosedimentometry (DCP). DCP analyses were conducted using a CPS Instruments Ltd. Disk centrifuge model 24000. Particle densities were determined by helium pycnometry prior to DCP analysis. A density gradient was constructed from 24% to 8% sucrose solutions.[87] A 263 nm poly(vinyl chloride) latex provided by the instrument manufacturer was used as a calibration standard prior to the analysis of each sample. Typical running times were between 10 and 15 min at a centrifugation rate of 20 000 rpm. The sucrose gradient was changed after characterizing each protein-nanoparticle conjugate to prevent excess serum albumin from interfering with subsequent studies.[81,82] All data were processed using the CPS Disk Centrifuge Control System (version 9.5, CPS Instruments Ltd.).

Field Emission Scanning Electron Microscopy (FE SEM). FE SEM samples were prepared by drying a droplet (10 μL) of highly dilute aqueous polypyrrole dispersion directly onto an aluminum stub (Agar Scientific). Analyses were conducted using a FEI Inspect field emission microscope operating at 5 to 7 kV. Because of the high electrical conductivity of polypyrrole, all FE SEM samples could be imaged directly without recourse to gold sputtering. Mean particle diameters were determined using ImageJ (version 1.42q, National Institute of Health, USA).

Transmission Electron Microscopy (TEM). Samples were prepared by drying an aqueous droplet (5 μL) of a highly dilute polypyrrole dispersion onto a carbon-coated grid (from Agar Scientific) and air-dried overnight before analysis using a Philips CM100 electron microscope operating at 100 kV.

X-ray Photoelectron Spectroscopy (XPS). With the exception of PPy bulk powder, all samples were prepared by drying a 200 μL aqueous droplet onto a silicon wafer at room temperature. PPy bulk powder was prepared for XPS analysis by mounting the dry powder onto a double-sided carbon adhesive tape; excess powder was shaken off prior to analysis. XPS analysis was conducted using a Kratos Axis Ultra DLD X-ray photoelectron spectrometer equipped with a monochromatic Al X-ray source operating at 6 mA and 15 kV at a base pressure of less than 10^{-8} Torr. The step size was 0.5 eV for the survey spectra (pass energy = 160 eV) and 0.05 eV for high resolution core-line spectra (pass energy = 80 eV). Typical acquisition times were 20 min for each survey spectrum and 30 min for each high resolution core-line spectrum. XPS spectra were processed using CasaXPS software pack (version 2.3.15).

Elemental Microanalysis. Polypyrrole samples were freeze-dried before elemental microanalysis. Elemental microanalyses were conducted in the Microanalysis Laboratory in the School of Chemistry at The University of Manchester (UK). Carbon, hydrogen, nitrogen, and sulfur contents were determined using a Carlo Erba EA1108 2400 elemental analyzer. Chlorine contents were determined separately using a Metrohm potentiometric autotitrator.

Helium Pycnometry. Polypyrrole nanoparticles were freeze-dried from aqueous solution prior to solid-state density measurements using a Micrometric Accu Pyc 1330 helium pycnometer conducted at 25 °C.

Solids Content Measurement. The solids content of purified aqueous dispersions of polypyrrole nanoparticles was

determined by gravimetry using an Ohaus MB45 Moisture Analyzer balance. All measurements were performed in triplicate.

Circular Dichroism (CD) Spectroscopy. CD spectra were recorded using a JASCO J-810 circular dichroism spectropolarimeter equipped with a Peltier temperature controller. All spectropolarimetric measurements were performed at 37 °C using a 2 mm path length quartz microcuvette (Suprasil, Hellma). Spectra were recorded at a scan rate of 15 nm per min using a 4 s response time and a bandwidth of 1 nm. Thermally denatured BSA was prepared by heating 375 nM BSA in 0.01 M HCl solution at 90 °C for 1 h. The CD spectrum of the denatured BSA was recorded within 2 h of its preparation. The concentrations of the diluted purified PPy–BSA core–shell nanoparticles (prepared using 200 mg/mL of PVAm-stabilized PPy nanoparticles and 673 μM BSA) and nonadsorbed BSA (isolated from the first centrifugation cycle) were spectroscopically quantified *via* a conventional UV–visible spectrophotometer (Perkin-Elmer Lambda 25 UV–visible spectrometer) prior to the CD measurements. The α-helix, β-sheet, β-turn, and random coil contents of each sample were calculated from the corresponding CD spectra (between 200 and 240 nm) using Kohonen's self-organizing map circular dichroism (SMOCD) protein secondary structure algorithm.[113]

Electrostatic Potential Distribution Calculation. The water-accessible space-filling model and Poisson–Boltzmann electrostatics (charge distribution) was calculated for human serum albumin crystallized from poly(ethylene glycol) 4000 (Protein Data Bank code: 1AO6)[17b] using PDB2PQR software package.[127,128]

Salt/Surfactant Challenge. The colloidal stability of purified PPy–BSA core–shell nanoparticles dispersed in 0.1 M PBS was assessed by means of either a salt or a surfactant challenge. Briefly, NaCl (74.1. mg, 127 mmol) or SDS (216 mg, 0.75 mmol) were added to 1.50 mL of 200 μg/mL purified PPy–BSA core–shell nanoparticles to achieve final concentrations of 1.0 M NaCl or 0.50 M SDS. These salt/nanoparticle or surfactant/nanoparticle mixtures were immersed in an ultrasonic bath for 0.50 h prior to removal of any dissociated BSA *via* five centrifugation–redispersion cycles. The purified BSA-PPy core–shell nanoparticles were then characterized by DLS and aqueous electrophoresis.

Conflict of Interest: The authors declare no competing financial interest.

Supporting Information Available: Calculation of theoretical protein coverage; disk centrifuge photosedimetometry (DCP) analysis of BSA-coated core–shell nanoparticles. This material is available free of charge *via* the Internet at http://pubs.acs.org.

REFERENCES AND NOTES

1. Unger, E. C. How Can Superparamagnetic Iron Oxides Be Used To Monitor Disease and Treatment? *Radiology* **2003**, *229*, 615–616.
2. Bulte, J. W. M.; Kraitcham, D. L. Iron Oxide MR Contrast Agents for Molecular and Cellular Imaging. *NMR Biomed.* **2004**, *17*, 484–499.
3. The United States National Institute of Health, MedicalTrials.gov homepage, http://medicaltrials.gov/ct2/esults?term=nanoparticles/ (assessed Nov 1, 2011).
4. Wagner, V.; Dullaart, A; Bock, A.; Zweck, A. The Emerging Nanomedicine Landscape. *Nat. Biotechnol.* **2006**, *24*, 1211–1218.
5. Jokerst, J. V.; Gambhir, S. S. Molecular Imaging with Theranostic Nanoparticles. *Acc. Chem. Res.* **2011**, *44*, 1050–1060.
6. Eifler, A. C.; Thaxton, C. S. Nanoparticle Therapeutics: FDA Approval, Clinical Trials, Regulatory Pathways, and Case Study. *Methods Mol. Biol.* **2011**, *726*, 325–338.
7. Sanhai, W. R.; Sakamoto, J. H.; Canady, R. Seven Challenges for Nanomedicine. *Nat. Nanotechnol.* **2008**, *83*, 349–353.
8. Zhao, Y.; Nalwa, H. S. *Nanotoxicity—Interactions of Nanomaterials with Biological Systems*; American Scientific Publisher: California, U.S., 2007.
9. Brewer, S. H.; Glomm, W. R.; Johnson, M. C.; Knag, M. K.; Franzen, S. Probing BSA Binding to Citrate-Coated Gold Nanoparticles and Surfaces. *Langmuir* **2005**, *21*, 9303–9307.
10. Choi, J.; Park, J. C.; Nah, H.; Woo, S.; Oh, J.; Kim, K. M.; Cheon, G. J.; Chang, Y.; Yoo, J.; Cheon, J. A Hybrid Nanoparticle Probe for Dual-Modality Positron Emission Tomography and Magnetic Resonance Imaging. *Angew. Chem., Int. Ed.* **2008**, *47*, 6259–6262.
11. Lee, J.-H.; Lee, K.; Moon, S. H.; Lee, Y.; Park, T. G.; Cheon, J. All-In-One Target-Cell-Specific Magnetic Nanoparticles for Simultaneous Molecular Imaging and siRNA Delivery. *Angew. Chem., Int. Ed.* **2009**, *48*, 4174–4179.
12. Wang, X.; Xia, T.; Ntim, S. A.; Ji, Z.; George, S.; Meng, H.; Zhang, H.; Castranova, V.; Mitra, S.; Nel, A. E. Quantitative Techniques for Assessing and Controlling The Dispersion and Biological Effects of Multiwalled Carbon Nanotubes in Mammalian Tissue Culture Cells. *ACS Nano* **2010**, *4*, 7241–7252.
13. Wang, L.; Liu, Y.; Li, W.; Jiang, X.; Ji, Y.; Wu, X.; Xu, L.; Qui, Y.; Zhao, K.; Wei, T.; *et al.* Targeting of Gold Nanorods at the Mitochondria of Cancer Cells: Implications for Cancer Therapy. *Nano Lett.* **2011**, *11*, 772–780.
14. Tzeng, Y.-K.; Faklaris, O.; Chang, B.-M.; Kuo, Y.; Hsu, J.-H.; Chang, H.-C. Superresolution Imaging of Aalbumin-Conjugated Fluorescent Nanodiamonds in Cells by Stimulated Emission Depletion. *Angew. Chem., Int. Ed.* **2011**, *50*, 2262–2265.
15. Carter, D. C.; Ho, J. X. Structure of serum albumin. *Adv. Protein Chem.* **1994**, *45*, 153–203.
16. Corti, M.-M.; Guralnik, J. M.; Salive, M. E.; Sorkin, J. D. Serum Albumin Level and Physical Disability as Predictors of Mortality in Older Persons. *J. Am. Med. Assoc.* **1994**, *272*, 1036–1042.
17. Sugio, S.; Kashima, A.; Mochizuki, S.; Noda, M; Kobayshi, K. Crystal Structure of Human Serum Albumin at 2.5 Å Resolution. *Protein Eng.* **1999**, *12*, 439–446.
18. Peter, T. Serum Albumin. *Adv. Protein Chem.* **1985**, *37*, 161–245.
19. Kratz, F. Albumin as a drug carrier: Design of Prodrugs, Drug Conjugates and Nanoparticles. *J. Controlled Release* **2008**, *132*, 171–183.
20. Mathies, J. C. Evaluation of a New Device for Rapidly Separating Serum or Plasma from Blood. *Clin. Chem.* **1974**, *29*, 1573–1576.
21. Mendez, C. M.; McClain, C. J.; Marsano, L. S. Albumin Therapy in Clinical Practice. *Nutr. Clin. Pract.* **2005**, *20*, 314–320.
22. Jimenez, J. R.; Roca, M.; Vega, E.; Garcia, M. L.; Benitez, A.; Bajen, M.; Martin-Comin, J. Influence of Temperature on the Radiochemical Purity of ^{99m}Tc-colloidal Rhenium Sulphide for Use in Sentinel Node Localization. *Nucl. Med. Commun.* **2008**, *29*, 166–172.
23. Rink, T.; Heuser, T.; Fitz, H.; Schroth, H. J.; Weller, E.; Zippel, H. H. Lymphoscintigraphic Sentinel Node Imaging and Gramma Probe Detection in Breast Cancer with Tc-99m Nanocolloidal Albumin: Results of an Optimized Protocol. *Clin. Nucl. Med.* **2001**, *26*, 293–298.
24. Dhabuwala, A.; Lamerton, P.; Stubbs, R. S. Relationship of ^{99m}-technetium Labelled Macroaggregated Albumin (^{99m}Tc-MAA) Uptake by Colorectal Liver Metastases to Response Following Selective Internal Radiation Therapy (SIRT). *BMC Nucl. Med* **2005**, *5*, 7.
25. Takegami, K.; Kaneko, Y.; Watanabe, T.; Watanabe, S.; Maruyama, T.; Matsumoto, Y.; Nagawa, H. Heating and Coagulation Volume Obtained with High-Intensity Focused Ultrasound Therapy: Comparison of Perflutren Protein-Type A Microspheres and MRX-133 in Rabbits. *Radiology* **2005**, *237*, 132–136.
26. Kligman, A. M.; Papa, C. M. Albumin as an Antiwrinkling Cosmetic. *J. Soc. Cosmet. Chem.* **1965**, *16*, 557–562.
27. Babson, A. L.; Winnick, T. Protein Transfer in Tumor-Bearing Rats. *Cancer Res.* **1954**, *14*, 606–611.
28. Matsumura, Y.; Maeda, H. A New Concept for Macromolecular Therapeutics in Cancer Chemotherapy: Mechanism of Tumor Tropic Accumulation of Proteins and the Antitumor Agent Smancs. *Cancer Res.* **1986**, *46*, 6387–6392.

29. Stehle, G.; Sinn, H.; Wunder, A.; Schrenk, H. H.; Stewart, J. C.; Hartung, G.; Maier-Borst, W.; Heene, D. L. Plasma Protein (Albumin) Catabolism by the Tumor Itself-Implications for Tumor Metabolism and the Genesis of Cachexia. *Crit. Rev. Oncol.* **1997**, *26*, 77–100.
30. Goller, M. I.; Barthet, C.; McCarthy, G. P.; Corradi, R.; Newby, B. P.; Wilson, S. A.; Armes, S. P.; Luk, S. Y. Synthesis and Characterization of Surface-Aminated Polypyrrole–Silica Nanocomposites. *Colloid Polym. Sci.* **1998**, *276*, 1010–1018.
31. Mikhaylova, M.; Kim, D. K.; Berry, C. C.; Zagorodni, A.; Toprak, M.; Curtis, A. S. G.; Muhammed, M. BSA Immobilization on Amine-Functionalized Superparamagnetic Iron Oxide Nanoparticles. *Chem. Mater.* **2004**, *16*, 2344–2354.
32. Garion, T. Heterocoagulation as an Inclusion Coating Technique for Ceramic Composite Processing. *J. Am. Ceram. Soc.* **1992**, *75*, 514–518.
33. Matijevic, E. Uniform Inorganic Colloid Dispersions. Achievements and Challenges. *Langmuir* **1994**, *10*, 8–16.
34. Abend, S.; Bonnke, N.; Gutschner, U.; Lagaly, G. Stabilization of Emulsions by Heterocoagulation of Clay Minerals and Layered Double Hydroxides. *Colloid Polym. Sci.* **1998**, *276*, 730–737.
35. Islam, A. M.; Chowdhry, B. Z.; Snowden, M. J. Heteroaggregration in Colloidal Dispersions. *Adv. Colloid Interface Sci.* **1995**, *62*, 109–136.
36. Ottewill, R. H.; Schofield, A. B.; Waters, J. A.; Williams, N., St. J. Preparation of Core–Shell Polymer Colloid Particles by Encapsulation. *Colloid Polym. Sci.* **1997**, *275*, 274–283.
37. Balmer, J. A.; Mykhaylyk, O. O.; Armes, S. P.; Fairclough, J. P. A.; Ryan, A. J.; Gummel, J.; Murray, M. W.; Murray, K. A.; Williams, N. S. J. Unexpected Facile Redistribution of Adsorbed Silica Nanoparticles between Latexes. *J. Am. Chem. Soc.* **2010**, *132*, 2166–2168.
38. Balmer, J. A.; Le Cunff, E. C.; Armes, S. P.; Murray, M. W.; Murray, K. A.; Williams, N. S. When Does Silica Exchange Occur between Vinyl Polymer–Silica Nanocomposite Particles and Sterically Stabilized Latexes. *Langmuir* **2010**, *26*, 13662–13671.
39. Balmer, J. A.; Mykhaylyk, O. O.; Armes, S. P.; Fairclough, J. P. A.; Ryan, A. J.; Gummel, J.; Murray, M. W.; Murray, K. A.; Williams, N. S. J. Time-Resolved Small-Angle X-ray Scattering Studies of Polymer–Silica Nanocomposite Particles: Initial Formation and Subsequent Silica Redistribution. *J. Am. Chem. Soc.* **2011**, *133*, 826–837.
40. Currie, E. P. K.; Norde, W.; Stuart, M. A. Tethered Polymer Chains: Surface Chemistry and Their Impact on Colloid and Surface Properties. *Adv. Colloid Interface Sci.* **2003**, *100–102*, 205–265.
41. Cho, E. C.; Xie, J.; Wum, P. A.; Xia, Y. Understanding the Role of Surface Charges in Cellular Adsorption *versus* Internalization by Selectively Removing Gold Nanoparticles on the Cell Surface with a I_2/KI Etchant. *Nano Lett.* **2009**, *9*, 1080–1084.
42. Jin, J; Gu, Y.-J.; Man, C. W.-Y.; Cheng, J.; Xu, Z.; Zhang, Y.; Wang, H.; Lee, V. H.-Y.; Cheng, S. H.; Wong, W.-T. Polymer-Coated $NaYF_4$:Yb^{3+}, Er^{3+} Upconversion Nanoparticles for Charge-Dependent Cellular Imaging. *ACS Nano* **2011**, *5*, 7838–7847.
43. Biesinger, K. E.; Stokes, G. N. Effects of Synthetic Polyelectrolytes on Selected Aquatic Organisms. *J. Water. Pollut. Control Fed.* **1986**, *58*, 207–213.
44. Fischer, D.; Li, Y.; Ahlemeyer, B.; Kriegisteir, J.; Kissel, T. *In Vitro* Cytotoxicity Testing of Polycations: Influence of Polymer Structure on Cell Viability and Hemolysis. *Biomaterials* **2003**, *24*, 1121–1131.
45. Huggins, C.; Tapley, D. F.; Jensen, E. V. Sulphydryl-Disulphide Relationships in the Induction of Gels in Proteins by Urea. *Nature* **1951**, *167*, 592–593.
46. Maruyama, T.; Katoh, S.; Nakajima, M. Mechanism of Bovine Serum Albumin Aggregation During Ultrafiltration. *Biotechnol. Bioeng.* **2001**, *75*, 233–238.
47. McNeill, R.; Siudak, R.; Wardlaw, J. H.; Weiss, D. E. Electronic Conduction in Polymers. I. The Chemical Structure of Polypyrrole. *Aust. J. Chem.* **1963**, *16*, 1056–1075.
48. Wang, X.; Gu, X.; Yuan, C.; Chen, S.; Zhang, P.; Zhang, T.; Yao, J.; Chen, F.; Chen, G. Elevation of Biocompatibility of Polypyrrole *in Vitro* and *in Vivo*. *J. Biomed. Mater. Res. A.* **2004**, *68*, 411–422.
49. Fonner, J. M.; Forciniti, L.; Nquyen, H.; Byrne, J. D.; Kou, Y, F.; Syeda-Nawaz, J.; Schmidt, C. E. Biocompatibility Impactions of Polypyrrole Synthesis Techniques. *Biomed. Mater.* **2008**, *3*, 034124.
50. Ramanaviciene, A.; Kausaite, A.; Tautkus, S.; Ramanavicius, A. Biocompatibility of Polypyrrole Particles: An *in-Vivo* Study In Mice. *J. Pharm. Pharmacol.* **2007**, *59*, 311–315.
51. Guimard, N. K.; Gomez, N.; Schmidt, C. E. Conducting Polymers in Biomedical Engineering. *Prog. Polym. Sci.* **2007**, *32*, 876–921.
52. Bendrea, A. D.; Cianga, L.; Cianga, I. Review Paper: Progress in the Field of Conducting Polymers for Tissue Engineering Applications. *J. Biomater. Appl.* **2011**, *26*, 2–84.
53. Bjorklund, R. B.; Liedberg, B. Electrically Conducting Composites of Colloidal Polypyrrole and Methylcellulose. *J. Chem. Soc., Chem. Commun.* **1986**, 1293–1295.
54. Armes, S. P.; Vincent, B. Dispersion of Electrically Conducting Polypyrrole Particles in Aqueous Media. *J. Chem. Soc., Chem. Commun.* **1987**, 288–290.
55. Bjorklund, R. B. Kinetics of Pyrrole Polymerization in Aqueous Iron Chloride Solution. *J. Chem. Soc., Faraday Trans. 1* **1987**, *83*, 1507–1514.
56. Simmons, M. R.; Chaloner, P. A.; Armes, S. P. Synthesis of Colloidal Polypyrrole Particles Using Reactive Polymeric Stabilizers. *Langmuir* **1995**, *11*, 4222–4224.
57. Beadle, P. M.; Armes, S. P.; Greaves, S. J.; Watts, J. F. X-ray Photoelectron Spectroscopy Studies on Sterically-Stabilized Polypyrrole Particles. *Langmuir* **1996**, *12*, 1784–1788.
58. Simmons, M. R.; Chaloner, P. A.; Armes, S. P.; Greaves, S. J.; Watts, J. F. Synthesis and Characterization of Colloidal Polypyrrole Particles Using Reactive Polymeric Stabilizer. *Langmuir* **1998**, *14*, 611–618.
59. Masalles, C.; Llop, J.; Vinas, C.; Teixidor, F. Extraordinary Overoxidation Resistance Increase in Self-Doped Polypyrroles by Using Non-conventional Low Charge-Density Anions. *Adv. Mater.* **2002**, *14*, 826–829.
60. Bae, W. J.; Kim, K. H.; Jo, W. H.; Park, Y. H. A Water-Soluble and Self-Doped Conducting Polypyrrole Graft Copolymer. *Macromolecules* **2005**, *38*, 1044–1047.
61. Mumtaz, M.; Lecommandoux, S.; Cloutet, E.; Cramail, H. Synthesis of Calibrated Poly(3,4-ethylenedioxythiophene) Latexes in Aqueous Dispersant Media. *Langmuir* **2008**, *24*, 11911–11920.
62. Morgan, M; Fielding, L. A.; Armes, S. P. Synthesis and Characterization of Sterically-Stabilized Polypyrrole Particles Using a Chemically Reactive Poly(vinyl amine)-based Stabilizer. *Colloid Polym. Sci.*, **2012**, in press, doi: 10.1007/s00396-012-2678-y.
63. Pope, M. R.; Armes, S. P.; Tarcha, P. J. Specific Activity of Polypyrrole Nanoparticulate Immunoreagents: Comparision of Surface Chemistry and Immunobilization Options. *Bioconjugate Chem.* **1996**, *7*, 436–444.
64. Bai, M.-Y.; Cheung, Y.-J.; Wickline, S. A.; Xia, Y. Colloidal Hollow Spheres of Conducting Polymers with Smooth Surface and Uniform, Controllable Sizes. *Small* **2009**, *5*, 1747–1752.
65. Venkatram, S.; Robert, L. Contrast Agent. WO Patent WO/2000/015267.
66. Au, K. M.; Lu, Z.; Matcher, S. J.; Armes, S. P. Polypyrrole Nanoparticles: A Potential Optical Coherence Tomography Contrast Agent for Cancer Imaging. *Adv. Mater.* **2011**, *23*, 5792–5795.
67. Wuang, S. C.; Neoh, K. G.; Kang, E.-T.; Pack, D. W.; Leckband, D. E. Synthesis and Functionalization of Polypyrrole-Fe_3O_4 Nanoparticles for Applications in Biomedicine. *J. Mater. Chem.* **2007**, *17*, 3354–3362.
68. Chen, M.; Fang, X.; Tang, S.; Zheng, N. Polypyrrole Nanoparticles for High-Performance *in Vivo* Near-Infrared Photothermal Cancer Therapy. *Chem. Commun.* **2012**, *48*, 8934–8936.

69. Ge, J.; Neofytou, E.; Cahill, T. J., III; Beygui, R. E.; Zare, R. N. Drug Release from Electric-Field Responsive Nanoparticles. *ACS Nano* **2012**, *6*, 227–233.
70. Lacerda, S. H. D. P.; Park, J. J.; Meuse, C.; Pristinski, D.; Becker, M. L.; Karim, A.; Douglas, J. F. Interaction of Gold Nanoparticles with Common Human Blood Proteins. *ACS Nano* **2010**, *4*, 365–379.
71. Armes, S. P.; Miller, J. F.; Vincent, B. Aqueous Dispersion of Electrically Conducting Monodisperse Polypyrrole Particles. *J. Colloid Interface Sci.* **1987**, *118*, 401–416.
72. Zotti, G.; Zecchin, S.; Schiavon, G.; Louwet, F.; Groenendaal, L.; Crispin, X.; Osikowicz, W.; Salaneck, W.; Fahlman, M. Electrochemical and XPS Studies toward the Role of Monomeric and Polymeric Sulfonate Counterions in the Synthesis, Composition, and Properties of Poly(3,4-ethylenedioxythiophene). *Macromolecules* **2003**, *36*, 3337–3344.
73. Sumaru, K.; Matsuoka, H.; Yamaoka, H. Exact Evaluation of Characteristic Protonation of Poly(vinylamine) in Aqueous Solution. *J. Phys. Chem.* **1996**, *100*, 9000–9005.
74. Shi, L.; Berland, C. Acid-Labile Polyvinylamine Micro- and Nanogel Capsules. *Macromolecules* **2007**, *40*, 4635–4643.
75. Zhnag, X.; Bai, R. Surface Electric Properties of Polypyrrole in Aqueous Solutions. *Langmuir* **2003**, *19*, 10703–10709.
76. Markham, G.; Obey, T. M.; Vincent, B. The Preparation and Properties of Dispersions of Electrically-Conducting Polypyrrole Particles. *Colloids Surf.* **1990**, *51*, 239–253.
77. Slocik, J. M.; Stone, M. O.; Naik, R. R. Synthesis of Gold Nanoparticles Using Multfunctional Peptides. *Small* **2005**, *1*, 1048–1052.
78. Slocik, J. M.; Tam, F.; Halas, N. J.; Naik, R. R. Peptide-Assembled Optically Responsive Nanoparticle Complex. *Nano Lett.* **2007**, *7*, 1054–1058.
79. Tomczak, M. M.; Slocik, J. M.; Stone, M. O.; Naik, R. R. Biobased Approaches to Inorganic Material Synthesis. *Biochem. Soc. Trans.* **2007**, *35*, 512–515.
80. Slocik, J. M.; Govorov, A. O.; Naik, R. R. Photoactivated Biotemplated Nanoparticles as an Enzyme Mimic. *Angew. Chem. In. Ed.* **2008**, *47*, 5335–5339.
81. Walczyk, D.; Bombelli, F. B.; Monopoli, M. P.; Lynch, I.; Dawson, K. A. What the cell "sees" in Bionanoscience. *J. Am. Chem. Soc.* **2010**, *132*, 5761–5768.
82. Monopoli, M. P.; Walczyk, D.; Campbell, A.; Elia, G.; Lynch, I.; Bombelli, F. B.; Dawson, K. A. Physical-Chemical Aspects of Protein Corona: Relevance to *in Vitro* and *in Vivo* Biological Impacts of Nanoparticles. *J. Am. Chem. Soc.* **2011**, *133*, 2525–2534.
83. Fielding, L. A.; Mykhaylyk, O. O.; Armes, S. P.; Fowler, P. W.; Mittal, V.; Fitzpatrick, S. Correcting for a Density Distribution: Particle Size Analysis of Core−Shell Nanocomposite Particles Using Disk Centrifuge Photosedimentometry. *Langmuir* **2012**, *28*, 2536–2544.
84. Bondoc, L. L.; Fitzpatrick, S. *J.* Size Distribution Analysis of Recombinant Adenovirus Using Disc Centrifugation. *Ind. Microbiol. Biotechnol* **1998**, *20*, 317–322.
85. Rocker, C.; Potzl, M.; Zhang, F.; Parak, W. J.; Nienhaus, G. U. A Quantitative Fluorescence Study of Protein Monolayer Formation on Colloidal Nanoparticles. *Nat. Nanotechnol.* **2009**, *4*, 577–580.
86. Maffre, P.; Nienhaus, K.; Amin, F.; Parak, W. J.; Nienhaus, G. U. Characterization of Protein Adsorption onto FePt Nanoparticles Using Dual-Focus Fluorescence Correlation Spectroscopy. *Beilstein J. Nanotechnol.* **2011**, *2*, 374–383.
87. McEwen, C. R. Tables for Estimating Sedimentation Through Linear Concentration Gradients of Sucrose Solution. *Anal. Biochem.* **1967**, *20*, 114–149.
88. Sarparanta, M.; Bimbo, L. M.; Rytkönen, J.; Mäkilä, E.; Laaksonen, T. J.; Laaksonen, P.; Nyman, M.; Salonen, J.; Linder, M. B.; *et al*. Intravenous Delivery of Hydrophobin-Functionalized Porous Silicon Nanoparticles: Stability, Plasma Protein Adsorption and Biodistribution. *Mol. Pharm.* **2012**, *9*, 654–663.
89. Stolnik, S.; Illum, L.; Davis, S. S. Long Circulating Microparticulate Drug Carriers. *Adv. Drug Delivery Rev.* **1995**, *16*, 195–214.
90. Casala, E.; Pfaller, T.; Duschl, A.; Oostingh, G. J.; Puntes, V. F. Hardening of the Nanoparticle-Protein Corona in Metal (Au, Ag) and Oxide (Fe_3O_4, CoO, and CeO_2) Nanoparticles. *Small* **2011**, *7*, 3479–3486.
91. Zhang, Y.; Yang, M.; Portney, N. G.; Cui, D. C.; Budak, G.; Ozbay, E.; Ozkan, M.; Ozkan, C. Zeta Potential: A Surface Electrical Characteristics to Probe the Interaction of Nanoparticles with Normal and Cancer Human Breast Epithelial Cells. *Biomed. Microdevices* **2008**, *10*, 321–328.
92. Zhang, Y.; Yang, M.; Park, J.-H.; Singelyn, J.; Ma, H.; Sailor, M. J.; Ruoslahti, E.; Ozkan, M.; Ozkan, C. A Surface-Charge Study on Cellular-Uptake Behaviour of F3-Peptide-Conjugated Iron Oxide Nanoparticles. *Small* **2009**, *5*, 1990–1996.
93. Street, G. B.; Clarke, T. C.; Geiss, R. H.; Lee, V. Y.; Nazzal, A.; Pfluger, P.; Scott, J. C. Characterization of Polypyrrole. *J. Phys. (Paris)* **1983**, *C3*, 599–606.
94. Iucci, G.; Polzonetti, G.; Infante, G.; Rossi, L. XPS and FT-IR Spectroscopy Study of Albumin Adsorption on the Surface of a π-Conjugated Polymer Film. *Surf. Interface Anal.* **2004**, *36*, 724–728.
95. Militello, V.; Casarino, C.; Emanuele, A.; Giostra, A.; Pullara, F.; Leone, M. Aggregration Kinetics of Bovine Serum Studied by FTIR Spectroscopy and Light Scattering. *Biophys. Chem.* **2004**, *107*, 175–187.
96. Kato, H.; Nishikawa, O.; Matsui, T.; Honma, S.; Kokado, H. Fourier Transform Infrared Spectroscopy Study of Conducting Polymer Polypyrrole: Higher Order Structure of Electrochemically Synthesized Film. *J. Phys. Chem.* **1991**, *95*, 6014–6016.
97. Salloum, D. S.; Schlenoff, J. B. Protein Adsorption Modalities on Polyelectrolyte Multilayers. *Biomacromolecules* **2004**, *5*, 1089–1096.
98. Li, N.; Zeng, S.; He, L.; Zhong, W. Probing Nanoparticle−Protein Interaction by Capillary Electrophoresis. *Anal. Chem.* **2010**, *82*, 7460–7466.
99. Gordon, M. J.; Huang, X.; Pentoney, S. L.; Zare, R. N. Capillary Electrophoresis. *Science* **1988**, *242*, 224–228.
100. Huang, X.; Gordon, M. J.; Zare, R. N. Current-Monitoring Method for Measuring the Electroosmotic Flow Rate in Capillary Zone Electrophoresis. *Anal. Chem.* **1988**, *60*, 1837–1838.
101. Huang, X.; Zare, R.; Sloss, S.; Ewing, A. G. End-Column Detection for Capillary Zone Electrophoresis. *Anal. Chem.* **1991**, *63*, 189–192.
102. Colton, I. J.; Carbeck, J. D.; Rao, J.; Whitesides, G. M. Affinity Capillary Electrophoresis: A Physical-Organic Tool for Studying Interactions in Biomolecular Recognition. *Electrophoresis* **1998**, *19*, 367–382.
103. Chu, Y.-H.; Avila, L. Z.; Gao, J.; Whitesides, G. M. Affinity Capillary Electrophoresis. *Acc. Chem. Res.* **1995**, *28*, 461–468.
104. Hill, A. V. The Possible Effects of the Aggregation of the Molecules of Haemoglobin on Its Dissociation Curves. *J. Physiol.* **1910**, *40*, 4–7.
105. Goutelle, S.; Maurin, M.; Rougler, F.; Barbaut, X.; Bourguignon, N.; Ducher, M.; Maire, P. The Hill Equation: A Review of Its Capabilities in Pharmacological Modelling. *Clin. Pharmacol.* **2008**, *22*, 633–648.
106. Aili, D.; Mager, M.; Roche, D.; Steven, M. M. Hybrid Nanoparticle-Liposome Detection of Photpholipase Activity. *Nano Lett.* **2011**, *11*, 1401–1405.
107. Biggs, S.; Habgood, M.; Jameson, G. K.; Yan, Y.-D. Aggregate Structure Formed *via* A Bridging Flocculation Mechanism. *Chem. Eng. J.* **2000**, *80*, 13–22.
108. Balmer, J. A.; Armes, S. P.; Fowler, P. W.; Tarnai, T.; Gaspar, Z.; Murray, K. A.; Williams, N. S. J. Packing Efficiency of Small Silica Particles on Large Latex Particles: A Facile Route to Colloidal Nanocomposites. *Langmuir* **2009**, *25*, 5339–5347.
109. Venyaminov, S. Y.; Vassilenko, K. S. Determination of Protein Tertiary Structure Class from Circular Dichroism Spectra. *Anal. Biochem.* **1994**, *222*, 176–184.

110. Holm, N. K.; Jespersen, S. K.; Thomassen, L. V.; Wolff, T. Y.; Sehgal, P.; Thomsen, L. A.; Christiansen, G.; Andersen, C. B.; Knudsen, A. D.; Otzen, D. A. Aggregation and Fibrillation of Bovine Serum Albumin. *Biochim. Biophys. Acta* **2007**, *1774*, 1128–1138.
111. Miltiello, V.; Vetri, V.; Leone, M. Conformational Changes Involved in Thermal Aggregation Process of Bovine Serum Albumin. *Biophys. Chem.* **2003**, *105*, 133–141.
112. Vaiana, S. M.; Emanuele, A.; Palma-Vittorelli, M. B.; Palma, M. U. Irreversible Formation of Intermediate BSA Oligomers Requires and Induces Conformation Changes. *Proteins: Structure, Function, and Bioinformatics* **2004**, *55*, 1053–1062.
113. Unneberg, P.; Merelo, J. J.; Chacon, P.; Moran, F. SOMCD: Method for Evaluating Protein Secondary Structure from UV Circular Dichroism Spectra. *Proteins: Structure, Function, and Genetics* **2001**, *42*, 460–470.
114. Fischer, N. O.; McIntosh, C. M.; Simard, J. M.; Rotello, V. M. Inhibition of Chymotrypsin through Surface Binding Using Nanoparticle-Based Receptor. *Proc. Natl. Acad. Sci. U.S.A.* **2002**, *99*, 5018–5023.
115. Srivastava, S.; Verma, A.; Frankamp, B. L.; Rotello, V. M. Controlled Assembly of Protein−Nanoparticle Composites through Protein Surface Recognition. *Adv. Mater.* **2005**, *17*, 617–621.
116. Shang, W.; Nuffer, J. H.; Dordick, J. S.; Siegel, R. W. Unfolding of Ribonuclease A on Silica Nanoparticles Surfaces. *Nano Lett.* **2007**, *7*, 1991–1995.
117. Laera, S.; Ceccone, G.; Rossi, F.; Gilliland, D.; Hussain, R.; Siligardi, G.; Calzolai, L. Measuring Protein Structure and Stability of Protein−Nanoparticle System with Synchrotron Radiation Circular Dichroism. *Nano Lett.* **2011**, *11*, 4480–4484.
118. Ladam, G.; Gergely, C.; Senger, B.; Decher, G.; Voegel, J.-C.; Schaaf, P.; Cuisinier, F. J. G. Protein Interactions with Polyelectrolyte Multilayers: Interactions between Human Serum Albumin and Polystyrene Sulfonate/Polyallylamine Multilayers. *Biomacromolecules* **2000**, *1*, 674–687.
119. Kirwan, L. J.; Papastavrou, G.; Borkovec, M.; Behrens, S. H. Imaging the Coil-to-Globule Conformation Transition of a Weak Polyelectrolyte by Tuning the Polyelectrolyte Charge Density. *Nano Lett.* **2004**, *4*, 149–152.
120. Ringler, P.; Schulz, G. E. Self-Assembly of Proteins into Designed Networks. *Science* **2003**, *302*, 106–109.
121. Hung, A.; Mwenifumbo, S.; Mager, M.; Kuna, J. J.; Stellacci, F.; Yarovsky, I.; Steven, M. M. Ordering Surface on the Nanoscale: Implications for Protein Adsorption. *J. Am. Chem. Soc.* **2011**, *133*, 1438–1450.
122. Champ, S.; Kock, O.; Ek, M.; Westman, E.; Wagberg, L. *Biocidal Coatings*. WO Patent 2008/055857, May 15, 2008.
123. Westman, E.-H.; Ek, M.; Enarsson, L.-E.; Wagberg, L. Assessment of Antibacterial Properties of Polvinylamine (PVAm) with Different Charge Densities and Hydrophobic Modifications. *Biomacromolecules* **2009**, *10*, 1478–1483.
124. Tajbakhsh, M.; Hosseinzadeh, R.; Alinezhad, H.; Ghahari, S.; Heydari, A.; Khaksar, S. Catalyst-free One-Pot Reductive Alkylation of Primary and Secondary Amines and *N*,*N*-Dimethylation of Amino Acid Using Sodium Borohydride in 2,2,2-Trifluoroethanol. *Synthesis* **2011**, *3*, 490–496.
125. Dal Caspm., T. A. An Evaluation of the Potential for Clandestine Manufacture of 3,4-Methylenedioxyamphetamine (MDA) Analogs and Homologs. *J. Forensic. Sci.* **1990**, *35*, 675–697.
126. Armes, S. P.; Vincent, B. J. Dispersions of Electrically Conducting Polypyrrole Particles in Aqueous Media. *J. Chem. Soc., Chem. Commun.* **1987**, 288–290.
127. Dolinsky, T. J.; Nielsen, J. E.; McCammon, J. A.; Baker, N. A. PDB2PQR: An Automated Pipeline for the Setup, Execution, and Analysis of Poisson-Boltzmann Electrostatics Calculations. *Nucleic Acid Res.* **2004**, *32*, W665–W667.
128. Dolinsky, T. J.; Czodrowski, P.; Li, H.; Nielsen, J. E.; Jensen, J. H.; Klebe, G.; Baker, N. A. PDB2PQR: Expanding and Upgrading Automated Preparation of Biomolecular Structures for Molecular Simulations. *Nucleic Acid Res.* **2007**, *35*, W522–W525.